Determination of indium melting curve at high pressure by picosecond acoustics

Simon Ayrinhac, Michel Gauthier, Marc Morand, Yiuri Garino, Silvia Boccato, Frédéric Decremps, Paraskevas Parisiades, Philippe Rosier, Nicki Siersch, Abderraouf Seghour, et al.

Determination of indium melting curve at high pressure by picosecond acoustics

Simon Ayrinhac,* Michel Gauthier, Marc Morand, Yiuri Garino, Silvia Boccato, Frédéric Decremps, Paraskevas Parisiades, Philippe Rosier,† Nicki C. Siersch, Abderraouf Seghour, and Daniele Antonangeli
Sorbonne Université, Muséum National d'Histoire Naturelle, UMR CNRS 7590, Institut de Minéralogie, de Physique des Matériaux et de Cosmochimie, IMPMC, 75005 Paris, France

Picosecond acoustics combined with diamond anvil cell is used to study liquid indium and to determine with high accuracy both the sound velocity and the melting curve over an extended pressure and temperature range. The sound velocities, determined by phonon surface imaging, complement previous inelastic X-ray scattering determinations and are in good agreement with estimations according to a thermodynamic model. Based on exact thermodynamic relations, the equation of state of the liquid phase is obtained using the isothermal bulk modulus $B_{T,0}$ and its first pressure derivative B'_T. These quantities are derived from the precise experimental determination of the variation of the sound velocity as a function of pressure. Melting is determined via the detection of abrupt changes in the elastic properties between solid and liquid phases and through the monitoring of the solid-liquid coexistence. The melting curve constrained up to 6 GPa and 673 K is shown to be well described by the Simon-Glatzel equation in the full (p,T) range explored.

Keywords: Picosecond Acoustics, Equation of State, Phase Diagram, High Pressure, Melting Curve, Sound velocity, Indium

I. INTRODUCTION

Determination of the thermoelastic properties of liquids at extreme conditions of pressure and temperature is fundamental for understanding the properties of condensed matter (*e.g.* [1, 2]), with direct implications in geophysics and planetary sciences (*e.g.* [3–6]). Even though it is an experimentally challenging task, many previous studies dealt with the determination of phase diagrams, including melting curves, equations of state or sound velocities measurements in the liquid phase, in addition with other thermodynamic properties determination such as bulk modulus or thermal expansion. In particular, many techniques were developed to measure the melting curves (see [7, 8] for a review). Early methods were based on visual observations [9, 10], existence of a temperature plateau [11], or on changes in electrical resistivity [12]. More recent *in situ* diagnostics include the appearance of diffuse signal in X-ray diffraction [13, 14], characteristic changes in the X-ray absorption spectroscopy [15] and detection by Synchrotron Mossbauer Spectroscopy experiments [16].

During the last decades, picosecond acoustics (PA) combined with diamond anvil cell (DAC) has been increasingly used to measure the thermoelastic properties of liquids and solids as well as their phase diagram. Nowadays, the combination of these two techniques appears to be a powerful and versatile laboratory tool [17] used to accurately measure both the melting curve and the sound velocities under high temperature and pressure conditions [18–20]. So far, PA has been successfully applied to study various solids (*e.g.* ice [21, 22], Ar [23], H [24]) and liquids (*e.g.* Hg [25, 26], Ga [18], Rb [20], Cs [19]).

To further explore the detection and metrology capabilities of PA, liquid indium can be considered a very interesting case study. First of all, its properties are very well known at ambient pressure [27, 28], making In a standard calibration substance [29, 30]. In particular, its melting temperature is a secondary reference point of the international temperature scale (ITS) [31]. Secondly, due to its low melting temperature, its ductility and low chemical reactivity [32], In can be routinely handled in the laboratory. Thirdly, although there are many papers on the measurements of sound velocities in liquid indium at high temperatures and ambient pressure (see for example the review of Blairs [33]), experimental data at gigapascal pressures are very scarce. To the best of our knowledge, the sound velocities at high pressure were measured only by Coppens *et al.* [34] up to around 0.01 GPa, and by Alatas *et al.* [35] and Komabayashi *et al.* [36] up to 6.7 GPa. Finally, the phase diagram of solid indium appears to be unusual compared to other III-A group elements (Al, Ga, Tl) and has attracted interest over time [37–41]. At ambient conditions, indium crystallizes in a tetragonal distortion of the compact cubic FCC system. This face-centered tetragonal structure (FCT) is stable at ambient temperature up to 50 GPa [41]. The c/a ratio is observed to reach a maximum value around 20 GPa [37, 41], which is related to an increased distortion of the FCT structure with respect to FCC. Above 50 GPa a solid-solid transition occurs and the In structure changes from FCT to a face-centered orthorombic (FCO) arrangement, stable up to ≈150 GPa [41]. The In phase diagram was also explored by *ab initio* electronic structure calculations at T=0 K [42], and at high temperatures by XRD (T>500 K) [43], but no other transitions were reported in the solid phase up to 247 GPa [41]. From

* simon.ayrinhac@sorbonne-universite.fr
† Present address: Université Paris-Saclay, CNRS UMR 9012, Laboratoire de Physique des 2 Infinis Irène Joliot-Curie (IJCLab), 91405 Orsay, France

all the above, we can conclude that In is particularly stable at high pressure and temperature compared to other metallic elements [44].

Regarding the liquid phase, although the melting point is well known at ambient pressure, the melting curve measured by several authors with different techniques shows significant discrepancies above 4 GPa [45]. The knowledge of the melting curve is actually crucial as it is used as a calibration curve at high p and high T (see for example reference [36]). This calls for a new set of experimental data obtained using a state of the art technique, with a particular attention dedicated to both the detection criteria of the solid-liquid transition, and the accurate pressure and temperature metrology.

Sound velocities in solids and liquids are markedly different and changes in sound velocities are a very sensitive probe to detect a solid-liquid phase transition [18, 46, 47] or subtle transformations in the liquid phase [19, 20]. Furthermore, accurate velocity measurements allow to derive useful thermodynamical quantities and to obtain the equation of state of the liquid [48, 49]. We have thus reexamined the properties of liquid indium in the temperature range 420-680 K and from ambient pressure to 6 GPa by PA technique combined with an externally heated diamond anvil cell (hDAC).

II. EXPERIMENTAL METHODS AND SET-UP

A. Picosecond acoustics set-up

Picosecond acoustics is a time-resolved, pump-probe, optical technique that generates and detects propagating strain waves in solids or liquids [50, 51].

In our set-up, the infrared beam from a mode-locked Ti:sapphire laser ($\lambda = 800$ nm, pulse width 100 fs, repetition rate ≈80 MHz *i.e.* 12.548(4) ns) is divided into a pump and a probe beam (see Fig. 1).

The pump beam passes through an acousto-optic modulator (AOM), which modulates the intensity of the pump beam around 1 MHz, to improve the signal-to-noise ratio through lock-in detection (HF2LI from Zurich Instruments). Then the pump beam is focused onto one of the surfaces of the sample (beam waist ≈ 1.5 μm), and, for metallic samples as the case of present interest, directly absorbed. The so-generated thermal stress relaxes and an acoustic wave propagates into the sample.

The probe beam is delayed with respect to the pump by a mechanical delay line (optical length 4 m, maximum delay time 13.33 ns) and focused on the opposite surface of the sample to detect its reflectivity changes due to the arrival of the acoustic wave.

These changes in reflectivity can be detected on the variation either in the intensity or in the phase of the reflectivity signal. The intensity variation $\rho = \mathrm{Re}\,(\Delta R/R)$ is related to the photoeleastic properties of the sample. Unfortunately, the photoelastic variation induced in indium is very small and a reflectivity measurement set-up is not efficient enough in this case. An interferometric system should be used instead.

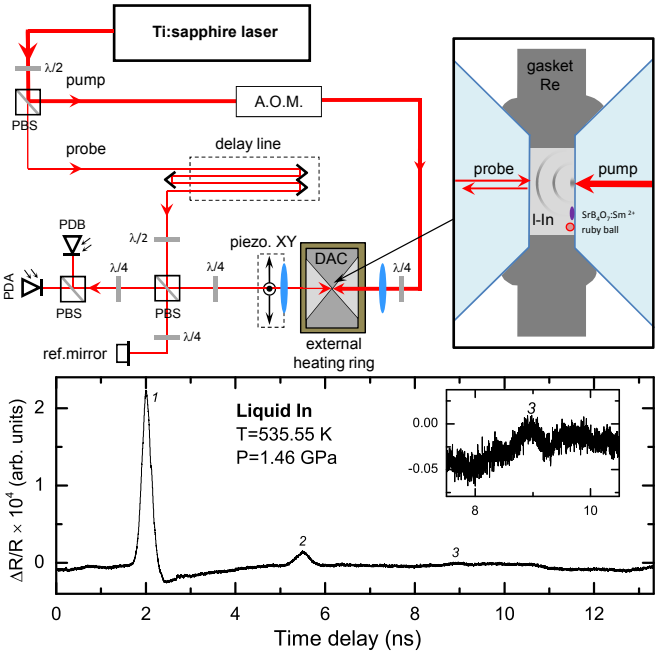

FIG. 1. (Top) Schematic view of the set-up. PBS: polarizing beamsplitter, $\lambda/2$: half-wave plate, $\lambda/4$: quarter-wave plate, PD: amplified photodetector, A.O.M. stands for acousto-optic modulator, and ref. mirror for reference mirror as a part of a Michelson interferometer. Blue ellipses represents optical objectives.
(Bottom) Interferometric signal as a function of delay time obtained in liquid In at high pressure and temperature with collinear pump and probe beams. Numbers identify consecutive echoes corresponding to the n^{th} wave arriving at the sample surface on the probe side. (Inset) Magnification of the third echo.

By means of a beam splitter, the probe beam is divided in two. One part is focused on the sample with the use of an objective mounted on a XY piezoelectric stage (P-517.2CL from Physik Instrumente) exploited to scan the sample surface over a 100×100 μm^2 area and collect surface phonon imaging data [52]. The remaining part of the probe beam is reflected on a reference mirror mounted on a piezoactuator with a feedback loop to stabilize the Michelson interferometer [53, 54]. The two beams reflected by the sample and the reference mirror are then mixed to obtain interferences before being collected by two amplified photodetectors. The voltage difference $V_A - V_B$ between the two photodetectors (PDA and PDB in Fig. 1) is proportional to the phase change of the relative reflectivity variation $\phi = \mathrm{Im}\,(\Delta R/R)$. The obtained signal shown in Fig. 1 (bottom) is thus affected by both the sample surface displacement and its refractive index variations through photoelastic effect [51].

B. Metrology : determination of pressure and temperature

Measurements are performed in a restively-heated diamond anvil cell, equipped with a pair of diamonds with culets of 600 μm and a pre-indented rhenium gasket. The large culets are chosen to facilitate surface phonon imaging as a sample with a diameter larger than 100 μm and thickness of tens of microns is needed. Heating is achieved by an external resistive heater ring, whose power is controlled by the target temperature measured by a K-type thermocouple located between the DAC and the resistive heater, and tuned by a PID controller. A second thermocouple is glued in contact with one of the diamonds.

The indium sample (127 μm thick foil from Sigma-Aldrich Chemie GmbH, purity 99.99% metal basis) is loaded at ambient conditions in a hole drilled in the rhenium gasket with a diameter of 340 μm and a thickness around 50 μm (a scheme of the sample chamber can be visualized in Fig. 1). The indium sample entirely fills the hole and plays both the role of metallic transducer and pressure transmitting medium when in the liquid state. Even when solid, being a soft metal, it does not sustain strong uniaxial stress and this deviatoric stress vanishes each time the sample melts.

Sm-doped strontium tetraborate (SrB_4O_7:Sm^{2+}) optical sensor is used as *in situ* pressure gauge [55], as the shift of the $^7D_0 - ^5F_0$ fluorescence line depends on the applied pressure but is almost independent of temperature. In addition, a ruby sphere (3000 ppm Cr-doped corundum: Al_2O_3:Cr^{3+}) [56] is placed inside the sample chamber and, in this case, the shift of the luminescence signal is sensitive to both p and T [57].

The fluorescence signal of the two calibrants is excited by a CW Sapphire Laser from Coherent Inc operating at $\lambda = 488$ nm.

The combined use of the two *in-situ* sensors allows not only to probe pressure, but as well to perform an independent check of the T-values measured by the thermocouple. In practice, being almost insensitive to T, the shift in the signal of the Sm-doped strontium tetraborate directly provides the pressure. The temperature can then be determined by the ruby calibrant by imposing in the signal analysis the pressure determined from the Sm-doped strontium tetraborate (see [58], section I).

As shown in Fig. 2, there is an excellent agreement between the temperature provided by the thermocouple glued to the diamond and the temperature estimated from the *in-situ* sensors according the two models. Unfortunately the ruby sphere disappeared inside the liquid before performing measurements at the highest isotherm (680 K). However, since the value of temperature given by the thermocouple was proven reliable for all other temperatures, this has been used for all the $p-T$ measurements.

The uncertainty on temperature measurements from the thermocouple is evaluated to be $\pm 2K$ and on pressure measurements determined from Sm-doped strontium tetraborate calibrant to be $0.1 - 0.2$ GPa.

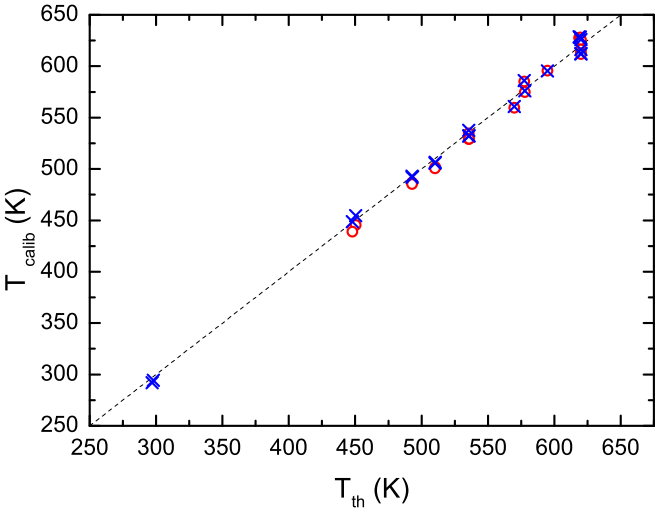

FIG. 2. Temperature estimated from the *in-situ* optical sensors T_{calib} (see text and [58], section I) as a function of the temperature value T_{th} provided by the thermocouple glued to one of the diamonds of the DAC. The analysis of the ruby fluorescence line shift is performed according to two models, Datchi [55] (red empty circles) and McCumber [59] (blue crosses). The equality relation is indicated by the dashed line.

III. EXPERIMENTAL RESULTS

A. Sound velocity measurements

Sound velocity measurements are performed through the analysis of the patterns detected by surface imaging and their evolution as a function of the delay time (*i.e.* producing a "movie") [18]. In liquid state, as in any elastically isotropic medium, phonon imaging patterns are circles, growing as a function of time, due to the arrivals of the spherical wavefronts generated by the focused pump beam at the opposite side of the sample (see the set-up at Fig. 1).

An integrated profile is obtained from each image and then all the profiles are stacked as a function of time to produce a figure showing growing circles as a function of time (see Fig. 3). The theoretical expression of the radius as a function of time $R(t)$ is obtained by the following set of equations [18]

$$\begin{aligned} z(t) &= v\,(t + mT_{laser} - \tau)\,, \\ e_0 &= v(t_0 + mT_{laser} - \tau), \\ R(t) &= \sqrt{(z - e_0)\,((2\,C(z) - z) + e_0)} \end{aligned} \tag{1}$$

where $C(z) = z\left[1 + \left(\frac{z_R}{z}\right)^2\right]$, v is the compressional sound velocity, $T_{laser} = 12.548(4)$ ns is the period between two subsequent pump laser shots, m is an integer

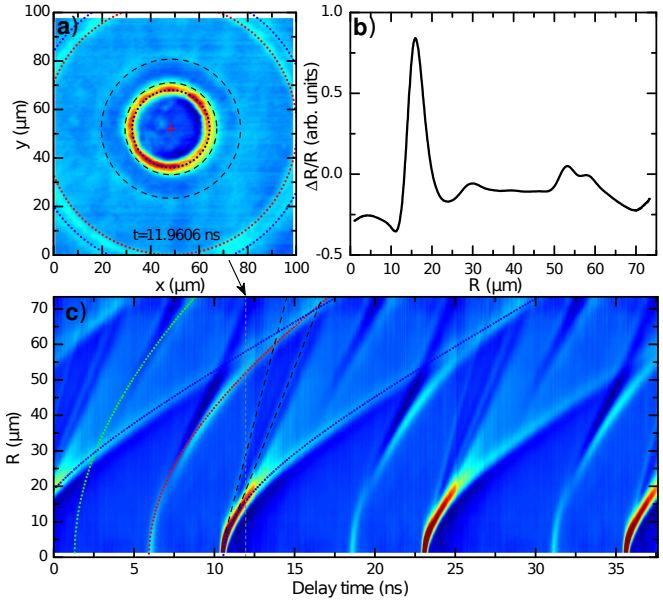

FIG. 3. a) Phonon imaging pattern of the acoustic wavefront at the liquid-diamond interface in liquid indium at 3 GPa and 682 K with collinear pump and probe at circular pattern center for 11.9606 ns a pump-probe delay. b) Integrated profile. c) Integrated profiles stacked versus time. For clarity, the final image between 0 and T_{laser} is duplicated 3 times. The colored ripples and the lines show the radius of the circles detected at the sample surface versus time. The nonlinear $R(t)$ curves are linked to the volume waves propagating inside the sample and appearing at the surface, whereas the linear $R(t)$ curves are due to the pure surface waves (possibly surface skimming bulk waves propagating in the diamond at the interface diamond-sample [60]). Only the first nonlinear curve is fitted by the function $R(t)$, and the calculation with the obtained results is shown as the blue dotted line. The red and green dotted lines are calculations corresponding to multiple reflections in the sample ($n = 2$ and $n = 3$ respectively) and demonstrate the quality of the fit procedure.

which accounts of the number of shots between generation and detection, $\tau = 0.329$ ns is the pump-probe coincidence time that depends on the optical path difference between probe and pump beams, e_0 is the sample thickness, t_0 is the emergence time of the wave, and z_R is the acoustic Rayleigh length. A typical value of z_R is 15 μm but it depends on the quality of the pump beam focusing on the sample surface. In the case where the thickness of the sample e_0 is larger than z_R, Eq. 1 greatly simplifies as [26]

$$R(t) = v\sqrt{z(t)^2 - e_0^2}. \qquad (2)$$

Parameters to be determined by the fitting process are then v, t_0 and z_R. These are fixed or left free, depending on the features of each movie. The evolution of the radius of the second (n=2) and third (n=3) waves are not fitted, but calculated replacing e_0 by $(2n-1)\,e_0$. With this method, the thickness e_0 and the sound velocity v are independently determined. The sound velocity data here obtained as a function of p and T are shown in Fig. 4 ([58], section II.A) . Uncertainty on sound velocity is evaluated to be around 25 m/s.

Sound velocity data at ambient pressure as a function of temperature are numerous in literature and are reviewed by Blairs [33] (compiling refs. [34, 61–66] and Fig.S3 in [58]).

On the contrary, sound velocity measurements as a function of pressure are scarce. Coppens [34] performed pioneering measurements but only up to 1500 psi, *i.e.* around 0.01 GPa. More recently, Alatas *et al.* [35] and Komabayashi *et al.* [36] measured the sound velocities by inelastic X-ray scattering through the fit of the phonon dispersion curve $\omega(Q)$ [67]. Alatas *et al.* [35] measured sound velocity for only 3 data points up to 4.0 GPa and 633 K. Komabayashi *et al.* [36] extended the $p-T$ range up to 923 K and 6.7 GPa. These data are however scattered, with large error bars, and, for clarity are not shown in Fig. 4 where our data set is compared to the velocities obtained from the EOS [36].

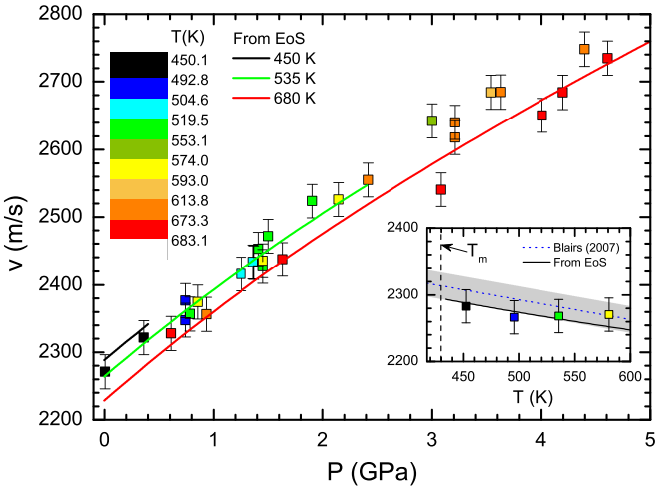

FIG. 4. Sound velocity in liquid indium as a function of pressure and temperature, measured by the phonon imaging method. The data are compared with velocities derived from the thermal EOS of Komabayashi [36] calculated along three reference isotherms. (Inset) Sound velocity as a function of temperature at ambient pressure, measured by the phonon imaging method (average thickness $e_0 = 68.3(12)$ μm, with imposed parameter $z_R = 16.2(4)$ μm) above melting temperature (T_M). The data are compared with the average linear relation of Blairs [33] (blue dotted line) and its dispersion (grey area, see Fig.S3 in [58]), and with the sound velocity calculated from the thermal EOS.

The sound velocity is linked to the adiabatic bulk modulus B_S and the density ρ via the relation

$$v = \sqrt{B_S/\rho}, \qquad (3)$$

then our measurements can be compared with values derived using the Komabayashi density-pressure-

temperature relation [36] which requires only 6 thermoelastic parameters to calculate sound velocity: the density at ambient pressure ρ_0, the isothermal bulk modulus $B_{T,0}$, the pressure derivative of the isothermal bulk modulus $B'_{T,0} = (\partial B_T/\partial p)_{p=0}$, the thermal expansion α_0, the Anderson-Grüneisen parameter δ_T [68] and the Grüneisen parameter γ_G.

The density ρ is obtained from the isothermal Vinet equation of state (EOS) [69]

$$p = 3B_{T,0}\left(\frac{1-x}{x^2}\right)e^{\eta(1-x)} \text{ with } \eta = \frac{3}{2}(B'_{T,0}-1) \quad (4)$$

where $x = (\rho/\rho_0)^{-1/3}$.

The thermal expansion α is calculated at any p and T using the Anderson-Grüneisen parameter δ_T

$$\alpha = \alpha_0 x^{3\delta_T} \quad (5)$$

leading to the thermal EOS $\rho(p,T)$

$$\rho = \rho_0 e^{-\alpha(T-T_M)} \quad (6)$$

from which the bulk modulus is derived as

$$B_T = \rho\left(\frac{\partial p}{\partial \rho}\right)_T \quad (7)$$

and finally the adiabatic bulk modulus is obtained as

$$B_S = B_T\left(1+\alpha\gamma_G T\right). \quad (8)$$

Despite its simplicity, this model based on simpler assumptions than other thermal EOS formalisms (see for example Ref. [70]) well accounts for the thermodynamic quantities at ambient pressure when using parameters given in Ref. [36] from the seminal work of Kamioka [46] : $\rho_0 = 7031.11$ kg/m^3, $B_{T,0} = 32.8$ GPa, $B'_{T,0} = 5.5$, $\alpha_0 = 12\ 10^{-5}$ K^{-1}, $\delta_T = 5.5$, and $\gamma_G = 2.5$.

As shown in Fig. 4 this EOS, associated with previous inelastic X-ray scattering data [35, 36], provide a good test of our experimental determination of the sound velocity at high pressure.

Previous authors provided a data review and an accurate evaluation of thermodynamic quantities at ambient pressure: $v(T)$ [33], $\rho(T)$ [27] and $C_p(T)$ [71] (fitted by a third order polynomial in Ref. [49]).

Following the seminal work of Shaw and Caldwell [72], these data combined with the present accurate determination of $(dv/dP)_{T,p=0} = 121(6)$ m.s^{-1}.GPa^{-1}, considered independent of the temperature, offer the opportunity to accurately calculate $B_{T,0}(T)$ and $B'_{T,0}(T)$ and to revise the equation of state up to $\approx$ 10 GPa. All the thermodynamic equations used are detailed in [58], section II.C. The calculated data are shown in Table I and are in very good agreement with Kamioka [46], with the notable exception for α_0 and B_T which must be be revised by approximately -10% and +4% respectively ([58], Fig.S4).

Finally the equation of state of liquid In is calculated from the thermodynamic parameters given in Table I and the isothermal Vinet EOS for each temperature. The results shown in Fig. 5 are close to Komabayashi [36].

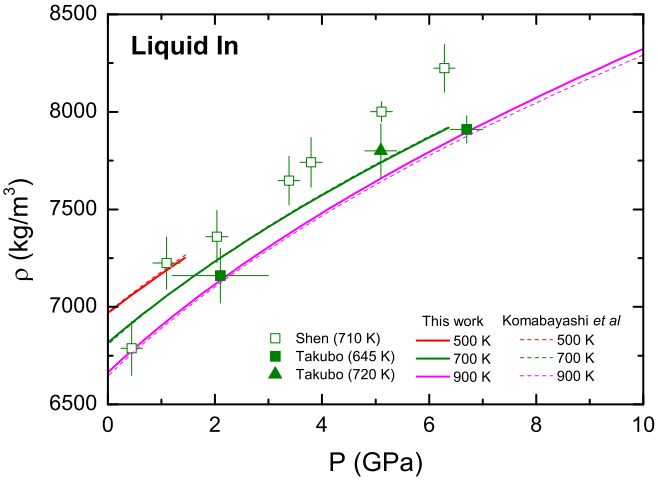

FIG. 5. Equation of state in liquid In calculated from the Vinet EOS and thermodynamic parameters given in table I (solid lines) compared to the EOS of Komabayashi (dashed lines). The experimental data are from Shen [73] and Takubo [74].

B. Determination of the melting curve

In this work, the melting of In was determined using two different methods. The first method is the detection of the isothermal solid-liquid phase transition through a large difference in the delay time of the arrival of the first echo, direct consequence of the changes in the sample thickness and mainly in the sound velocity upon transition [18], (see Fig. 6). The melting line was crossed along isotherms for increasing and decreasing pressures. This method is very accurate since the sound velocity is very sensitive to modifications in long-range order and consequently in the thermodynamic properties of the material. Noteworthy, the liquid-solid transition is always accompanied by a "plateau" in the curve of the sample pressure p as a function of membrane pressure p_m likely consequence of the volume variation at the transition ([58], Fig.S5).

The second method is the tracking of pressure and temperature for which liquid and solid phases coexist in equilibrium, and follow this along the melting line [75, 76]. Here, we remember that according to the Gibbs phase rule, for a single component system, T and p are not independent when two phases are in coexistence, as along the melting line (only one degree of freedom). The experimental protocol starts with measurements in the liquid, and then the temperature is continuously decreased (at a rate around 1 K/s). When the melting temperature is reached, the pressure in the sample chamber decreases due to volume reduction of the sample due to partial solidification. Further volume reduction in both coexisting solid and liquid is expected due to the temperature decrease. These aspects favor the decrease in p concomitant to the imposed decrease in T along the melting line.

TABLE I. Thermodynamic data of liquid In calculated from reference data $v(T)$, $\rho(T)$, $C_p(T)$, and the value of $(dv/dp)_{T,p=0}$ determined in this work.

T	v	ρ	C_p	α_0	B_T	dB_T/dT	$B_T^{'}$	δ_T	γ_G
K	m/s	kg/m^3	J/kg.K	10^{-5}K^{-1}	GPa	MPa/K	-	-	-
T_M^0	2313.93	7022.00	258.0	10.85	34.02	-20.26	5.25	5.49	2.25
450	2307.90	7006.57	257.4	10.88	33.62	-20.01	5.25	5.47	2.25
500	2293.00	6968.47	256.0	10.93	32.63	-19.40	5.24	5.44	2.25
550	2278.10	6930.37	254.8	11.00	31.68	-18.81	5.23	5.40	2.24
600	2263.20	6892.27	253.8	11.06	30.75	-18.23	5.22	5.36	2.23
650	2248.30	6854.17	252.9	11.12	29.85	-17.66	5.21	5.32	2.22
700	2233.40	6816.07	252.2	11.18	28.98	-17.11	5.20	5.28	2.21
750	2218.50	6777.97	251.6	11.24	28.14	-16.58	5.19	5.24	2.20
800	2203.60	6739.87	251.2	11.31	27.33	-16.07	5.18	5.20	2.19
850	2188.70	6701.77	250.8	11.37	26.53	-15.59	5.16	5.17	2.17
900	2173.80	6663.67	250.4	11.44	25.77	-15.12	5.15	5.13	2.16
950	2158.90	6625.57	250.1	11.50	25.02	-14.68	5.14	5.10	2.14
1000	2144.00	6587.47	249.8	11.57	24.30	-14.26	5.13	5.07	2.13

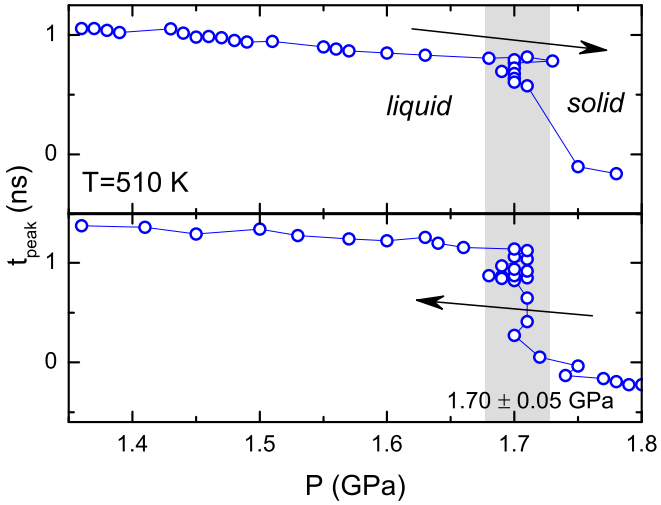

FIG. 6. Transition between liquid and solid indium (grey region) as recorded by the large and sharp variation of the arrival time of the first acoustic echo at T=510 K. The transition pressure, measured both for increasing p (top panel) and decreasing p (bottom panel), is in this case 1.70(5) GPa.

However, due to the non transparency of the sample, the visual observation of the solid-fluid equilibrium is impossible. The full transition of the sample into the solid is thus checked by three ways ([58], Fig.S7). Firstly, the pressure stops to decrease although the temperature continues to decrease. Secondly, the transition from liquid to solid is observed by phonon imaging of the surface, with the apparition of non circular patterns due to the elastic anisotropy of solid indium. Thirdly, a large shift of the delay time of the echo peak is observed at the transition (similarly to what shown in Fig. 6 as travel time modification upon phase transition is quite higher than the variations due only to the temperature or the pressure in the liquid phase, see also Fig.S7 in [58]).

The compilation of the measurements done by the two methods are presented in Fig. 7. The melting line is fitted by the widely used Simon-Glatzel equation [77]

$$T_M\,(p) = T_{ref}\left[\frac{p-p_{ref}}{a}+1\right]^{1/c}, \qquad (9)$$

where $p_{ref} = 0$ GPa, $T_{ref} = T_M^0 = 429.74850(34)$ K are the well known values used as secondary point of the international temperature scale (ITS) [30, 31] and the two adjustable parameters a and c have been found to be $a = 4.61(11)$ GPa and $c = 1.792(34)$.

In order to check the consistency of our data, we can compare the slopes of the meting line at ambient pressure κ obtained by the Simon-Glatzel relation (see Eq. 10) and by the Clausius-Clapeyron relation (see Eq. 11).

From the Simon-Glatzel relation we obtain

$$\kappa = \left(\frac{dT_M}{dp}\right)_{p=0} = \frac{T_M^0}{ac} = 52.0(16)\ \text{K/GPa}. \qquad (10)$$

This value is higher than the values given by Jayaraman *et al.* (Table 3 in Ref. [79]) ranging from 43 to 50 K/GPa.

The Clausius-Clapeyron relation gives the slope of the melting line at ambient pressure as

$$\kappa_{ref} = \frac{T_M^0(V_{m,liq}-V_{m,sol})}{\Delta H_{m,M}}. \qquad (11)$$

where V_m are molar volumes in liquid and solid, and $\Delta H_{m,M}$ is the molar enthalpy of fusion (or melting). The quantities entering this relation measured at T_M and ambient pressure are carefully reviewed ([58], section III.B).Here we emphasize that the largest source of uncertainty in κ_{ref} comes from the value of ΔV_m, which is crucial to evaluate the consistency of the data [80]. Resulting $\kappa_{ref} = 53.1(48)$ K/GPa is in agreement with κ determined from the Simon-Glatzel relation.

To summarize, our determination of κ is in agreement with previous published values and gives further confidence in the reliability of our temperature measurements.

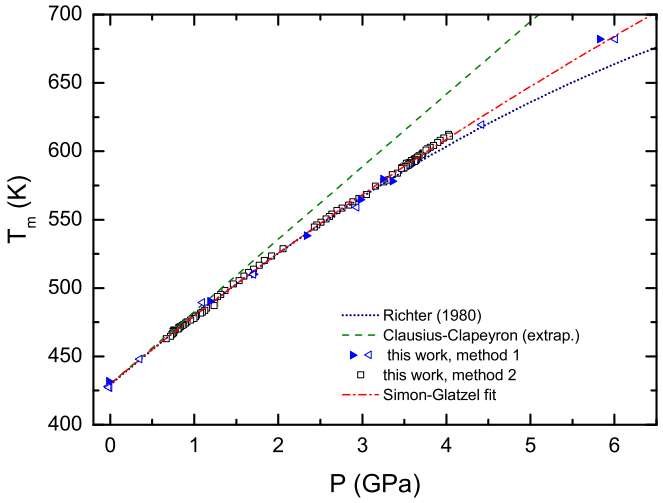

FIG. 7. Indium melting line measured by picosecond acoustics. As explained in the text, experimental (p,T) points are obtained in two ways. Method 1) large and sharp shift of the arrival time of the first acoustic echo upon pressure increase (blue solid triangles) and upon pressure decrease (blue empty triangles) along isothermal paths; Method 2) through monitoring the liquid-solid equilibrium (empty black squares). All the data are fitted by a Simon-Glatzel equation (dash-dotted red line, see text and Eq. 9). In addition, an extrapolation of the Clausius Clapeyron relationship at ambient pressure is shown (Eq. 11, green line), as well as the polynomial function given by Richter extrapolated above 3.5 GPa (black dotted line, see Table 1 in ref. [78]).

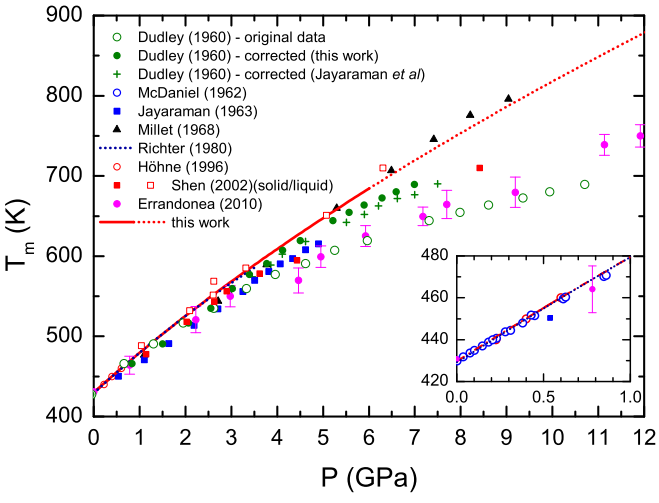

FIG. 8. The melting curve obtained in this work by picosecond acoustics (red line) and extrapolated above 6 GPa (red dotted line) is compared with the literature data: Dudley (1960) [32], Dudley corrected in this work, McDaniel (1962) [81], Jayaraman *et al.* (1963) [79] and their correction of the Dudley data, Millet (1968) [82] (data points are taken from Cannon (1974) [83]), Richter (1980) [78], Höhne (1996) [84], Shen (2002) [85] (red filled squares: solid, red empty squares: liquid), and Errandonea (2010) [45]. The inset shows the low pressure region.

IV. DISCUSSION

The melting curve obtained in the present study and extrapolated up to 12 GPa, pressure up to which no anomaly is expected in the liquid, is compared to literature data in Fig. 8.

The disagreement between our data and the melting curve recently proposed by Errandonea [45] is evident for pressures above 3 GPa. In this work a Bridgman-type cell was employed up to 12 GPa and melting was identified as a drop in the resistance, measured with the 4-point technique, which is a well proven melting criterion. Concerning metrology, the pressure scale used in their work relies on a calibration curve relating loading pressure and sample pressure, which is linear and well constrained by many reference points [86]. On the contrary, in the Bridgman pressure apparatus used, the temperature was measured by a thermocouple located 500 μm away from the center. Therefore temperature gradients could explain an underestimated temperature, to a larger extent to what claimed by the authors (less than 25 K[45]). In further support of these remarks, the slope at ambient pressure of melting curve determined by Errandonea is $\kappa = 45.2$ K/GPa, is much lower than the expected reference value $\kappa_{ref} = 53.1(48)$ K/GPa and lower than our determination ($\kappa = 52.0(16)$ K/GPa).

Recently, Ma *et al.* [87] propose an agreement with the measurements of Errandonea. However this model is based on two experimental (p,T) data of the melting curve, which were directly taken from the measurements of Errandonea. Such a low melting temperature is also supported by the values of Dudley [32]. However this work used an outdated pressure scale, subsequently proven to be inaccurate. Specifically, the Ba I-II transition pressure was assumed according to Bridgman [88], with $p_{Ba\ I-II} = 77.4$ katm $= 7.843$ GPa, while the revised value $p_{Ba\ I-II} = 5.50(5)$ GPa at 295.15 K was established in the subsequent work of Haygarth *et al.* [89]. In addition, Decker made a careful review (see Table 7 in the Ref. [90] and related discussion) including the data of Haygarth and some other studies resulting in $p_{Ba\ I-II} = 5.53(12)$ GPa at 298.15 K. Based on this revised value, the calibration curve of Dudley can be corrected ([58], section III.C). The melting curve of Dudley before and after the correction is shown in Fig. 8. The so-corrected melting curve is in agreement with our data.

Richter [78] performed measurements in piston-cylinder up to 3.5 GPa and determined the melting curve by the differential thermal analysis (DTA) technique, carefully corrected for asymmetrical friction, and by the volumetric technique. The results obtained by the two techniques are consistent and yield to a melting curve modelled according to a least-square fit as $T_M = 156.0 + 52.6p - 2.25p^2$ where p is in GPa, and T_M is in Celsius. Our data at low pressure are in excel-

lent agreement with these measurements, as well as with results of McDaniel *et al.* [81], and Höhne *et al.* [84].

Our data are extrapolated at pressures above 6 GPa according to the Eq. 9. This extrapolation is in agreement with the melting temperatures of Shen measured by X-ray diffraction (XRD) [85], and in good agreement with Millet [82], despite the uncertainties of these measurements highlighted by Cannon [83].

V. CONCLUSION

In this work the phase diagram and the thermoelastic properties of liquid indium have been accurately investigated over an extended pressure and temperature range by picosecond acoustics measurements in combination with resistively-heated diamond anvil cells. Particular care was devoted to the associated metrology. Indium was observed to be a very stable metallic compound at high pressure and high temperature, both in its solid and liquid phases. The thermodynamic properties of the liquid phase, well documented at ambient pressure as a function of temperature, have been here implemented to simultaneous high pressure and high temperature conditions, according to well established thermodynamic formulations built on precise sound velocity measurements performed along selected isotherms. A p-ρ-T EOS for the liquid has been also derived.

The liquid-solid transition was determined through a clear and unambiguous criterium: the jump in time-of-flight measurements that directly relates to the changes of thermoelastic properties between the two phases. We have also constrained the melting curve by monitoring the liquid-solid equilibrium along several experimental runs. Results obtained by the two methods are consistent, and the measurements are in good agreement with the thermoelastic references values of indium at ambient pressure.

Thanks to the careful metrology of pressure and temperature, our data offer an accurate determination of the melting curve, and the $T_M(p)$ line could be used as a calibration curve for future investigations.

Besides the specific interest of the case of indium, our study shows the reliability and versatility of picosecond acoustic technique and associated methods, opening to the study of more complex or reactive liquid systems such as the alkali metals, sulfur or phosphorus. Furthermore, since sound velocity is highly sensitive to the changes of the thermoelastic parameters, a similar approach can be used to probe first-order transitions other than melting, as well as more subtle transitions related to progressive changes in structure. Finally, studies can be extended over a larger pressure and temperature range using more performing resistive-heating systems rather than the simple external heater employed in this study. Experiments exploiting local or internal heaters for example can reach temperatures up to 1100-1300 K (*e.g.* [91, 92]). Moreover, temperatures higher than 1000 K can be achieved by laser heating.

VI. ACKNOWLEDGMENTS

This project has received funding from the European Research Council (ERC) under the European Union's Horizon 2020 research and innovation Programme (grant agreement No. 724690). Femtosecond laser micromachining at IMPMC has been developed and realized by the "Cellule Project" with the financial support of ANR 2010-JCJC-604- 01. Authors wish to thank also Yoann Guarnelli for his help in DAC preparation.

[1] H.-K. Mao, X.-J. Chen, Y. Ding, B. Li, and L. Wang, Solids, liquids, and gases under high pressure, Reviews of Modern Physics **90**, 015007 (2018).
[2] H. Tanaka, Liquid–liquid transition and polyamorphism, The Journal of Chemical Physics **153**, 130901 (2020).
[3] F. D. Stacey, High pressure equations of state and planetary interiors, Reports on progress in physics **68**, 341 (2005).
[4] G. Morard, J. Bouchet, A. Rivoldini, D. Antonangeli, M. Roberge, E. Boulard, A. Denoeud, and M. Mezouar, Liquid properties in the Fe-FeS system under moderate pressure: Tool box to model small planetary cores, American Mineralogist: Journal of Earth and Planetary Materials **103**, 1770 (2018).
[5] H. Terasaki, A. Rivoldini, Y. Shimoyama, K. Nishida, S. Urakawa, M. Maki, F. Kurokawa, Y. Takubo, Y. Shibazaki, T. Sakamaki, *et al.*, Pressure and composition effects on sound velocity and density of core-forming liquids: Implication to core compositions of terrestrial planets, Journal of Geophysical Research: Planets **124**, 2272 (2019).
[6] F. Xu, G. Morard, N. Guignot, A. Rivoldini, G. Manthilake, J. Chantel, L. Xie, A. Yoneda, A. King, E. Boulard, *et al.*, Thermal expansion of liquid Fe-S alloy at high pressure, Earth and Planetary Science Letters **563**, 116884 (2021).
[7] S. Anzellini and S. Boccato, A practical review of the laser-heated diamond anvil cell for university laboratories and synchrotron applications, Crystals **10**, 459 (2020).
[8] P. Parisiades, A review of the melting curves of transition metals at high pressures using static compression techniques, Crystals **11**, 416 (2021).
[9] Q. Williams, R. Jeanloz, J. Bass, B. Svendsen, and T. J. Ahrens, The melting curve of iron to 250 gigapascals: A constraint on the temperature at Earth's center, Science **236**, 181 (1987).
[10] R. Boehler, Temperatures in the Earth's core from melting-point measurements of iron at high static pressures, Nature **363**, 534 (1993).

[11] O. T. Lord, E. T. Wann, S. A. Hunt, A. M. Walker, J. Santangeli, M. J. Walter, D. P. Dobson, I. G. Wood, L. Vočadlo, G. Morard, *et al.*, The NiSi melting curve to 70 GPa, Physics of the Earth and Planetary Interiors **233**, 13 (2014).

[12] R. Boehler, The phase diagram of iron to 430 kbar, Geophysical Research Letters **13**, 1153 (1986).

[13] G. Morard, D. Andrault, N. Guignot, J. Siebert, G. Garbarino, and D. Antonangeli, Melting of Fe-Ni-Si and Fe-Ni-S alloys at megabar pressures: implications for the core-mantle boundary temperature, Physics and Chemistry of Minerals **38**, 767 (2011).

[14] S. Anzellini, A. Dewaele, M. Mezouar, P. Loubeyre, and G. Morard, Melting of iron at Earth's inner core boundary based on fast x-ray diffraction, Science **340**, 464 (2013).

[15] S. Boccato, R. Torchio, S. Anzellini, E. Boulard, F. Guyot, T. Irifune, M. Harmand, I. Kantor, F. Miozzi, P. Parisiades, *et al.*, Melting properties by x-ray absorption spectroscopy: common signatures in binary Fe-C, Fe-O, Fe-S and Fe-Si systems, Scientific reports **10**, 1 (2020).

[16] J. M. Jackson, W. Sturhahn, M. Lerche, J. Zhao, T. S. Toellner, E. E. Alp, S. V. Sinogeikin, J. D. Bass, C. A. Murphy, and J. K. Wicks, Melting of compressed iron by monitoring atomic dynamics, Earth and Planetary Science Letters **362**, 143 (2013).

[17] F. Decremps, M. Gauthier, S. Ayrinhac, L. Bove, L. Belliard, B. Perrin, M. Morand, G. L. Marchand, F. Bergame, and J. Philippe, Picosecond acoustics method for measuring the thermodynamical properties of solids and liquids at high pressure and high temperature, Ultrasonics **56**, 129 (2015).

[18] S. Ayrinhac, M. Gauthier, G. L. Marchand, M. Morand, F. Bergame, and F. Decremps, Thermodynamic properties of liquid gallium from picosecond acoustic velocity measurements, Journal of Physics: Condensed Matter **27**, 275103 (2015).

[19] F. Decremps, S. Ayrinhac, M. Gauthier, D. Antonangeli, M. Morand, Y. Garino, and P. Parisiades, Sound velocity and equation of state in liquid cesium at high pressure and high temperature, Physical Review B **98**, 184103 (2018).

[20] S. Ayrinhac, V. N. Robinson, F. Decremps, M. Gauthier, D. Antonangeli, S. Scandolo, and M. Morand, High-pressure transformations in liquid rubidium, Phys. Rev. Materials **4**, 113611 (2020).

[21] M. Kuriakose, S. Raetz, Q. M. Hu, S. M. Nikitin, N. Chigarev, V. Tournat, A. Bulou, A. Lomonosov, P. Djemia, V. E. Gusev, *et al.*, Longitudinal sound velocities, elastic anisotropy, and phase transition of high-pressure cubic H_2O ice to 82 GPa, Physical Review B **96**, 134122 (2017).

[22] S. Sandeep, T. Thréard, E. De Lima Savi, N. Chigarev, A. Bulou, V. Tournat, A. Zerr, V. E. Gusev, and S. Raetz, 3d characterization of individual grains of coexisting high-pressure H_2O ice phases by time-domain brillouin scattering, Journal of Applied Physics **130**, 053104 (2021).

[23] S. Raetz, M. Kuriakose, P. Djemia, S. M. Nikitin, N. Chigarev, V. Tournat, A. Bulou, A. Lomonosov, V. E. Gusev, and A. Zerr, Elastic anisotropy and single-crystal moduli of solid argon up to 64 GPa from time-domain brillouin scattering, Physical Review B **99**, 224102 (2019).

[24] A. F. Goncharov, M. Gauthier, D. Antonangeli, S. Ayrinhac, F. Decremps, M. Morand, A. Grechnev, S. M. Tretyak, and Y. A. Freiman, Elasticity and Poisson's ratio of hexagonal close-packed hydrogen at high pressures, Phys. Rev. B **95**, 214104 (2017).

[25] F. Decremps, L. Belliard, B. Couzinet, S. Vincent, P. Munsch, G. Le Marchand, and B. Perrin, Liquid mercury sound velocity measurements under high pressure and high temperature by picosecond acoustics in a diamond anvils cell, Review of Scientific Instruments **80**, 073902 (2009).

[26] S. Ayrinhac, M. Gauthier, L. E. Bove, M. Morand, G. Le Marchand, F. Bergame, J. Philippe, and F. Decremps, Equation of state of liquid mercury to 520 K and 7 GPa from acoustic velocity measurements, The Journal of Chemical Physics **140**, 244201 (2014).

[27] M. J. Assael, I. J. Armyra, J. Brillo, S. V. Stankus, J. Wu, and W. A. Wakeham, Reference data for the density and viscosity of liquid cadmium, cobalt, gallium, indium, mercury, silicon, thallium, and zinc, Journal of Physical and Chemical Reference Data **41**, 033101 (2012).

[28] B. B. Alchagirov, R. K. Dadashev, F. F. Dyshekova, and D. Z. Elimkhanov, The surface tension of indium: Methods and results of investigations, High Temperature **52**, 920 (2014).

[29] D. G. Archer and S. Rudtsch, Enthalpy of fusion of indium: a certified reference material for differential scanning calorimetry, Journal of Chemical & Engineering Data **48**, 1157 (2003).

[30] H. Abe, National standard and new reference material for specific heat capacity measurements, Analytical Sciences **37**, 201 (2021).

[31] H. Preston-Thomas, The international temperature scale of 1990 (ITS-90), metrologia **27**, 3 (1990).

[32] J. D. Dudley and H. T. Hall, Experimental fusion curves of indium and tin to 105000 atmospheres, Physical Review **118**, 1211 (1960).

[33] S. Blairs, Review of data for velocity of sound in pure liquid metals and metalloids, International materials reviews **52**, 321 (2007).

[34] A. B. Coppens, R. T. Beyer, and J. Ballou, Parameter of nonlinearity in fluids III. Values of sound velocity in liquid metals, The Journal of the Acoustical Society of America **41**, 1443 (1967).

[35] A. Alatas, H. Sinn, J. Zhao, A. H. Said, B. M. Leu, W. Sturhahn, E. E. Alp, G. Shen, and V. B. Prakapenka, Experimental aspects of inelastic x-ray scattering studies on liquids under extreme conditions (P-T), High Pressure Research **28**, 175 (2008).

[36] T. Komabayashi, J. Kato, K. Hirose, S. Tsutsui, S. Imada, Y. Nakajima, and A. Q. Baron, Temperature dependence of the velocity-density relation for liquid metals under high pressure: Implications for the Earth's outer core, American Mineralogist **100**, 2602 (2015).

[37] K. Takemura, Effect of pressure on the lattice distortion of indium to 56 GPa, Phys. Rev. B **44**, 545 (1991).

[38] O. Schulte and W. B. Holzapfel, Effect of pressure on atomic volume and crystal structure of indium to 67 GPa, Phys. Rev. B **48**, 767 (1993).

[39] K. Takemura and H. Fujihisa, High-pressure structural phase transition in indium, Phys. Rev. B **47**, 8465 (1993).

[40] A. Mikhaylushkin, U. Häussermann, B. Johansson, and S. Simak, Fluctuating lattice constants of indium under

high pressure, Physical review letters **92**, 195501 (2004).
[41] Y. Akahama, K. Takahashi, K. Kamiue, T. Sugimoto, N. Hirao, and Y. Ohishi, Pressure-induced reentrant structural transition and equation of state of indium, Journal of Applied Physics **125**, 075901 (2019).
[42] G. Sin'ko and N. Smirnov, Structural transitions in indium under high pressure: Ab initio electronic structure calculations, Physical Review B **74**, 134113 (2006).
[43] G. Shen, N. Sata, M. L. Rivers, and S. R. Sutton, Melting of indium at high pressure determined by monochromatic x-ray diffraction in an externally-heated diamond anvil cell, Applied Physics Letters **78**, 3208 (2001).
[44] O. Degtyareva, Simple metals at high pressures, in *High-Pressure Crystallography* (Springer, 2010) pp. 261–280.
[45] D. Errandonea, The melting curve of ten metals up to 12 GPa and 1600 K, Journal of Applied Physics **108**, 033517 (2010).
[46] H. Kamioka, Change of ultrasonic wave velocity in indium near the melting point, Journal of the Physical Society of Japan **52**, 2784 (1983).
[47] L. Xu, Y. Bi, X. Li, Y. Wang, X. Cao, L. Cai, Z. Wang, and C. Meng, Phase diagram of tin determined by sound velocity measurements on multi-anvil apparatus up to 5 GPa and 800 K, Journal of Applied Physics **115**, 164903 (2014).
[48] C. Su, Y. Liu, Z. Wang, W. Song, P. D. Asimow, H. Tang, and H. Xie, Equation of state of liquid bismuth and its melting curve from ultrasonic investigation at high pressure, Physica B: Condensed Matter **524**, 154 (2017).
[49] S. Ayrinhac, Heat capacity ratio in liquids at high pressure, Journal of Applied Physics **129**, 185903 (2021).
[50] H. Maris, Picosecond ultrasonics, Scientific American **278**, 86 (1998).
[51] O. Matsuda, M. C. Larciprete, R. L. Voti, and O. B. Wright, Fundamentals of picosecond laser ultrasonics, Ultrasonics **56**, 3 (2015).
[52] Y. Sugawara, O. B. Wright, O. Matsuda, M. Takigahira, Y. Tanaka, S. Tamura, and V. E. Gusev, Watching ripples on crystals, Phys. Rev. Lett. **88**, 185504 (2002).
[53] B. Perrin, B. Bonello, J. Jeannet, and E. Romatet, Interferometric detection of hypersound waves in modulated structures, Prog. Natural Sci. **6**, S444 (1996).
[54] S. Zhang, E. Peronne, L. Belliard, S. Vincent, and B. Perrin, Three-dimensional acoustic wavefront imaging in anisotropic systems by picosecond acoustics, Journal of Applied Physics **109**, 033507 (2011).
[55] F. Datchi, A. Dewaele, P. Loubeyre, R. Letoullec, Y. Le Godec, and B. Canny, Optical pressure sensors for high-pressure–high-temperature studies in a diamond anvil cell, High Pressure Research **27**, 447 (2007).
[56] J. Chervin, B. Canny, and M. Mancinelli, Ruby-spheres as pressure gauge for optically transparent high pressure cells, International Journal of High Pressure Research **21**, 305 (2001).
[57] K. Syassen, Ruby under pressure, High Pressure Research **28**, 75 (2008).
[58] See supplemental material at [url inserted by publisher] for additional details .
[59] D. McCumber and M. Sturge, Linewidth and temperature shift of the r lines in ruby, Journal of Applied Physics **34**, 1682 (1963).
[60] N. Chigarev, P. Zinin, D. Mounier, A. Bulou, L. Ming, T. Acosta, and V. Gusev, Analysis of ultrasonic echoes induced by pulsed laser action on an iron film in a diamond anvil cell, High Pressure Research **30**, 78 (2010).
[61] O. Kleppa, Ultrasonic velocities of sound in some metallic liquids. adiabatic and isothermal compressibilities of liquid metals at their melting points, The Journal of Chemical Physics **18**, 1331 (1950).
[62] R. Turner, E. Crozier, and J. Cochran, A new technique for measuring the velocity of sound in liquid metals, Canadian Journal of Physics **50**, 2735 (1972).
[63] P.-E. Berthou and R. Tougas, The compressibilities of liquid Sn-Tl, In-Bi, Sn-In, Bi-Sb, and Bi-Cd-Tl alloys, Metallurgical and Materials Transactions B **3**, 51 (1972).
[64] D. Almond and S. Blairs, Ultrasonic speed, compressibility, and structure factor of liquid cadmium and indium, The Journal of Chemical Thermodynamics **12**, 1105 (1980).
[65] R. Bek, E. Nold, and S. Steeb, Röntgen-Beugungsuntersuchungen an Bi-In-Schmelzen (in german) : X-Ray diffraction experiments with Bi-In-melts, Zeitschrift für Naturforschung A **36**, 150 (1981).
[66] E. Pashuk and B. Pashaev, Temperature dependence of superround velocity and related volumetric dependence of the young modulus of some metals, Teplofizika Vysokikh Temperatur **21**, 479 (1983).
[67] D. Antonangeli, F. Occelli, H. Requardt, J. Badro, G. Fiquet, and M. Krisch, Elastic anisotropy in textured hcp-iron to 112 GPa from sound wave propagation measurements, Earth and Planetary Science Letters **225**, 243 (2004).
[68] F. Birch, Thermal expansion at high pressures, Journal of Geophysical Research (1896-1977) **73**, 817 (1968).
[69] P. Vinet, J. Ferrante, J. R. Smith, and J. H. Rose, A universal equation of state for solids, Journal of Physics C: Solid State Physics **19**, L467 (1986).
[70] K. D. Litasov, P. I. Dorogokupets, E. Ohtani, Y. Fei, A. Shatskiy, I. S. Sharygin, P. N. Gavryushkin, S. V. Rashchenko, Y. V. Seryotkin, Y. Higo, *et al.*, Thermal equation of state and thermodynamic properties of molybdenum at high pressures, Journal of Applied Physics **113**, 093507 (2013).
[71] T. W. Chapman, The heat capacity of liquid metals, Materials Science and Engineering **1**, 65 (1966).
[72] G. H. Shaw and D. A. Caldwell, Device for measuring sound speeds in reactive liquids at high pressure and temperature, Review of Scientific Instruments **56**, 1402 (1985).
[73] G. Shen, N. Sata, M. Newville, M. L. Rivers, and S. R. Sutton, Molar volumes of molten indium at high pressures measured in a diamond anvil cell, Applied physics letters **81**, 1411 (2002).
[74] Y. Takubo, H. Terasaki, T. Kondo, S. Mitai, S. Kamada, T. Kikegawa, and A. Machida, Development of density measurement for metals at high pressures and high temperatures using x-ray absorption imaging combined with externally heated diamond anvil cell, Comptes Rendus Geoscience **351**, 182 (2019), high-Pressure Mineral Physics Seminar(HPMPS-9, Saint-Malo, France, 24–28 September 2017).
[75] F. Datchi, P. Loubeyre, and R. LeToullec, Extended and accurate determination of the melting curves of argon, helium, ice (H_2O), and hydrogen (H_2), Physical Review B **61**, 6535 (2000).
[76] V. M. Giordano, F. Datchi, and A. Dewaele, Melting curve and fluid equation of state of carbon dioxide at high pressure and high temperature, The Journal of chemical

physics **125**, 054504 (2006).
[77] F. Simon and G. Glatzel, Remarks on fusion pressure curve, Z. Anorg. Allg. Chem **178**, 309 (1929).
[78] P. Richter and J. Clark, Asymmetrical friction in a piston-cylinder device and the effect on the melting curves of indium and bismuth, Review of Scientific Instruments **51**, 959 (1980).
[79] A. Jayaraman, W. Klement Jr, R. Newton, and G. Kennedy, Fusion curves and polymorphic transitions of the group iii elements aluminum, gallium, indium and thallium at high pressures, Journal of Physics and Chemistry of Solids **24**, 7 (1963).
[80] E. Y. Kulyamina, V. Y. Zitserman, and L. Fokin, Titanium melting curve: data consistency assessment, problems and achievements, Technical Physics **63**, 369 (2018).
[81] M. L. McDaniel, S. E. Babb, and G. J. Scott, Melting curves of five metals under high pressure, The Journal of Chemical Physics **37**, 822 (1962).
[82] L. E. Millet, *Experimental Melting Curves of Cadmium, Indium, Lead, Tin, and Zinc and Mössbauer Measurements in Iron to 90 Kilobars* (Brigham Young University, 1968).
[83] J. F. Cannon, Behavior of the elements at high pressures, Journal of Physical and Chemical Reference Data **3**, 781 (1974).
[84] G. Höhne, W. Dollhopf, K. Blankenhorn, and P. Mayr, On the pressure dependence of the heat of fusion and melting temperature of indium, Thermochimica acta **273**, 17 (1996).
[85] G. Shen, N. Sata, N. Taberlet, M. Newville, M. L. Rivers, and S. R. Sutton, Melting studies of indium: determination of the structure and density of melts at high pressures and high temperatures, Journal of Physics: Condensed Matter **14**, 10533 (2002).
[86] D. Errandonea, D. Martínez-García, A. Segura, J. Ruiz-Fuertes, R. Lacomba-Perales, V. Fages, A. Chevy, L. Roa, and V. Mũnoz-San José, High-pressure electrical transport measurements on p-type GaSe and InSe, High Pressure Research **26**, 513 (2006).
[87] J. Ma, W. Li, G. Yang, S. Zheng, Y. He, X. Zhang, X. Zhang, and X. Zhang, Modeling the pressure-dependent melting temperature of metals, Physics of the Earth and Planetary Interiors **309**, 106602 (2020).
[88] P. W. Bridgman, The resistance of 72 elements, alloys and compounds to 100000 Kg/cm^2, Proceedings of the American Academy of Arts and Sciences **81**, 167 (1952).
[89] J. Haygarth, I. Getting, and G. Kennedy, Determination of the pressure of the barium i-ii transition with single-stage piston-cylinder apparatus, Journal of Applied Physics **38**, 4557 (1967).
[90] D. L. Decker, W. Bassett, L. Merrill, H. Hall, and J. Barnett, High-pressure calibration: A critical review, Journal of Physical and Chemical Reference Data **1**, 773 (1972).
[91] D. Antonangeli, T. Komabayashi, F. Occelli, E. Borissenko, A. C. Walters, G. Fiquet, and Y. Fei, Simultaneous sound velocity and density measurements of hcp iron up to 93 GPa and 1100 K: An experimental test of the Birch's law at high temperature, Earth and Planetary Science Letters **331**, 210 (2012).
[92] Z. Du, L. Miyagi, G. Amulele, and K. K. Lee, Efficient graphite ring heater suitable for diamond-anvil cells to 1300 K, Review of Scientific Instruments **84**, 024502 (2013).

Determination of indium melting curve at high pressure by picosecond acoustics Supplementary Information

Simon Ayrinhac,* Michel Gauthier, Marc Morand, Yiuri Garino, Silvia Boccato, Frédéric Decremps, Paraskevas Parisiades, Philippe Rosier,† Nicki C. Siersch, Abderraouf Seghour, and Daniele Antonangeli
Sorbonne Université, Muséum National d'Histoire Naturelle, UMR CNRS 7590, Institut de Minéralogie, de Physique des Matériaux et de Cosmochimie, IMPMC, 75005 Paris, France
(Dated: October 25, 2022)

CONTENTS

I. Metrology: determination of pressure and temperature 2
A. SmSTB : a pressure sensor 2
B. Combined use of ruby and SmSTB: a pressure and temperature sensor 2

II. Sound velocity measurements 4
A. Sound velocity in liquid In determined by phonon imaging 4
B. Sound velocity in liquid In - review as a function of T 6
C. Thermodynamic relations used to deduce EOS for liquid In 7
D. Comparison of the equations of state at ambient pressure 8

III. Determination of the melting curve 9
A. Additional figures 9
B. Slope of the melting curve from the Clausius-Clapeyron relation 11
1. Physical and thermodynamical data 11
2. Liquid state 12
3. Solid state 12
4. Difference of the molar volumes 12
5. The Clausius-Clapeyron relation at ambient pressure 13
C. Correction of the melting curve from Dudley *et al* 14

References 15

* simon.ayrinhac@sorbonne-universite.fr
† Present address: Université Paris-Saclay, CNRS UMR 9012, Laboratoire de Physique des 2 Infinis Irène Joliot-Curie (IJCLab), 91405 Orsay, France

I. METROLOGY: DETERMINATION OF PRESSURE AND TEMPERATURE

In this work, pressure and temperature are accurately determined *in-situ*. Pressure is measured by analysis of the luminescence signal of the Sm-doped strontium tetraborate calibrant (noted SmSTB thereafter), while temperature is obtained by analysis of Cr-doped corundum (ruby) calibrant, both loaded inside the sample chamber of a diamond anvil cell (actually embedded in the liquid sample). An independent determination of the temperature is provided by a thermocouple glued on the side of one of the two diamonds in the DAC. The accuracy of the temperature reading of the thermocouple is confirmed by the temperature obtained *in-situ*.

A. SmSTB : a pressure sensor

The pressure determination via the shift of a luminescence signal is used since 1975 [36]. Syassen [43] made a review for ruby and shown that the more accurate expression can be written as a function of $\epsilon = \Delta\lambda/\lambda(p_0, T_0)$. Accordingly, pressure can be derived from the $^7D_0 \rightarrow {}^5F_0$ luminescence line of SmSTB (samarium-doped strontium tetraborate SrB_4O_7:Sm^{2+}) fitted to a single Voigt function. Following Datchi *et al.* [15, 16] the corresponding pressure p is derived according the following analytical form

$$p = A\epsilon\,(1 + B\epsilon)\,(1 + C\epsilon)^{-1} = A_1\Delta\lambda\left(\frac{1 + B_1\Delta\lambda}{1 + C_1\Delta\lambda}\right) \tag{1}$$

$$\text{with}\quad \Delta\lambda = \lambda(p, T_0) - \lambda(p_0, T_0) \tag{2}$$

where $\lambda(p, T_0)$ is the actual luminescence peak position at pressure p and temperature T_0 and $\lambda(p_0, T_0) = 685.437$ nm is our reference value of the luminescence line measured at ambient conditions ($p_0 = 0$ GPa, $T_0 = 296$ K) [15].

The 3 parameters, $A_1 = 3.989(6)$ GPa/nm, $B_1 = 6.915(74)\ 10^{-3}\text{nm}^{-1}$ and $C_1 = 16.6(10)\ 10^{-3}\text{nm}^{-1}$, extracted from Ref. [15] p. 454, have been determined using the "DO2007 ruby scale" [18] (see Eq. (6) in Ref. [15]).

Using $\lambda(p_0, T_0)$, if we compare the A, B et C coefficients of SmSTB $A_{Sm} = A_1\lambda(p_0, T_0) = 2734$ GPa, $B_{Sm} = B_1\lambda(p_0, T_0) = 4.74$, $C_{Sm} = C_1\lambda(p_0, T_0) = 11.4$ with those of ruby (see next section) $A_{ruby} = 1884$ GPa, $B_{ruby} = 5.5$ and $C_{ruby} = 0$, we note that the pressure sensitivity of SmSTB is close to those of ruby. Moreover, the $^7D_0 \rightarrow {}^5F_0$ luminescence line is a singlet and should be less sensitive to pressure gradients and temperature than the $^2E \rightarrow {}^4A_2$ R_1 line used for ruby calibrant.

In fact, at ambient pressure, the shift of the luminescence line of the SmSTB is basically temperature independent. To estimate the error due to neglecting the temperature, the Eq.(2) is modified as

$$\Delta\lambda(p, T) = \Delta\lambda_{p_0,T_0}(p) + \Delta\lambda_{P_0,T_0}(T) = \lambda(p, T_0) - \lambda(p_0, T_0) + \lambda(p_0, T) - \lambda(p_0, T_0). \tag{3}$$

Following Datchi *et al.* [15] we assume a quadratic form for $\Delta\lambda_{p_0,T_0}(T)$

$$\Delta\lambda_{p_0,T_0}(T) = A_2\Delta T + B_2\Delta T^2 + C_2\Delta T^3,\ \text{with}\ \Delta T = (T - T_0) \times 10^{-3}, \tag{4}$$

where A_2 = -87(12) 10^{-3} nm/K, $B_2 = 462(60)\ 10^{-3}$ nm/K^2, C_2 = -238(70) 10^{-3} nm/K^3 have been determined([1]) at $p = p_0$ and are supposed to be pressure independent.

In our temperature range the maximum pressure deviation is then around 0.05 GPa *i.e.* of the same order of magnitude of the experimental uncertainty on our pressure measurement.

In practice, for our purposes, the effect of temperature variation on λ and hence on the estimation of pressure from the above presented analysis of luminescence signal of the SmSTB calibrant can be considered negligible.

B. Combined use of ruby and SmSTB: a pressure and temperature sensor

The ruby calibrant, commonly used for pressure determination and in this paper, is a chromium-doped corundum (α-Al_2O_3:Cr^{3+}) with 3000 ppm Cr concentration. The pressure effects of the chromium concentration can be found in Ref [12], and a nice revue of ruby properties useful for high pressure community can be found in ref [43].

Differently from SmSTB, the lineshift of the $^2E \rightarrow {}^4A_2$ ruby luminescence signal depends both on pressure and temperature. Accordingly, from the combined use of the two calibrants we can get both pressure and temperature.

[1] This coefficients are different than those written in Ref.[15] because of a typo.

At first, pressure is determined using the SmSTB calibrant. The experimental lineshift of the ruby sensor is then corrected for the pressure effects by shifting it according to the determined pressure value. Temperature is finally obtained by analysis of the so-corrected lineshift.

The two lines R_1 and R_2 are fitted to Voigt profiles as a function of energy (cm^{-1}), with a linear background. Following Dorogokupets *et al.* [18] and revue in ref [43], pressure and wavelength λ_{R_1} are related, being:

$$p = A_4\epsilon\,(1 + B_4\epsilon) \quad \text{with} \quad \epsilon = \frac{\lambda_{R_1}(p, T_0) - \lambda_{R_1}(p_0, T_0)}{\lambda_{R_1}(p_0, T_0)} \tag{5}$$

where $A_4 = 1884$ GPa, $B_4 = 5.5$ and $\lambda_{R_1}(p_0, T_0) = 694.336$ nm is our reference value at ambient condition. This relation is generally used to derive pressure from ruby measurements. Here we use to re-scale lineshift for pressure effects.

As discussed in the main text, we used two methods to analyse the temperature dependence of the lineshift $\Delta\lambda_{R_1}$:

1. The first method is based on a phenomenological model [15] in which only the position of the maximum of the luminescence signal is determined, after data smoothing. At low temperatures, the R_1 and R_2 lines are well separated and the maximum is obvious equal to the position of the R_1 line. However at high temperatures the R_1 and R_2 lines get close and progressively merge. The temperature dependence of the ruby line is then described assuming 3 distinct regions, "low", "medium" and "high" temperatures, each one having a specific expression relating temperature to lineshift. In the present case our data belong to the "high" temperature region, where the dependence of the maximum position as a function of temperature is given by a polynomial function (Eq.(2) in Ref. [15])

$$\Delta\lambda_{R_1}(T) = A_3\Delta T + B_3\Delta T^2 + C_3\Delta T^3, \text{ with } \Delta T = (T - T_0) \times 10^{-3} \tag{6}$$

   with T_0 =296 K, A_3 = 7.46(4) nm/K, B_3 = -3.01(25) nm/K^2 and C_3 = 8.76(33) nm/K^3.

2. The second method is based on the ruby properties as described by McCumber *et al.* [33] treated according to the simplified approach proposed by Syassen [43].

Temperatures estimated according the two methods are within mutual uncertainties.

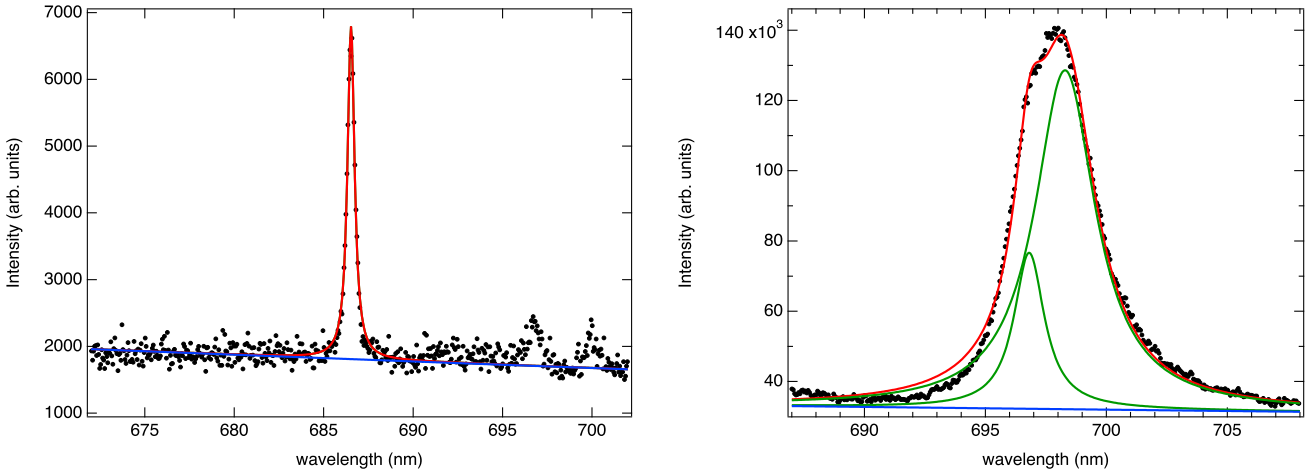

Supplementary Figure S1. (left) SmSTB luminescence signal fitted to a single Voigt profile (red line). According to Eq. (1-2) p=4.45 GPa. (right) Ruby luminescence signal fitted to two Voigt profiles (green lines), whose addition is shown as red line, and analysed according to McCumber model [33] with pressure imposed from the SmSTB determination, yielding to T_{calib}=612.5 K. Both measurements are performed on calibrants embedded in liquid indium at high pressure and T_{th}=619.95 K as determinated using a thermocouple glued on one of the diamonds of the high pressure cell.

II. SOUND VELOCITY MEASUREMENTS

A. Sound velocity in liquid In determined by phonon imaging

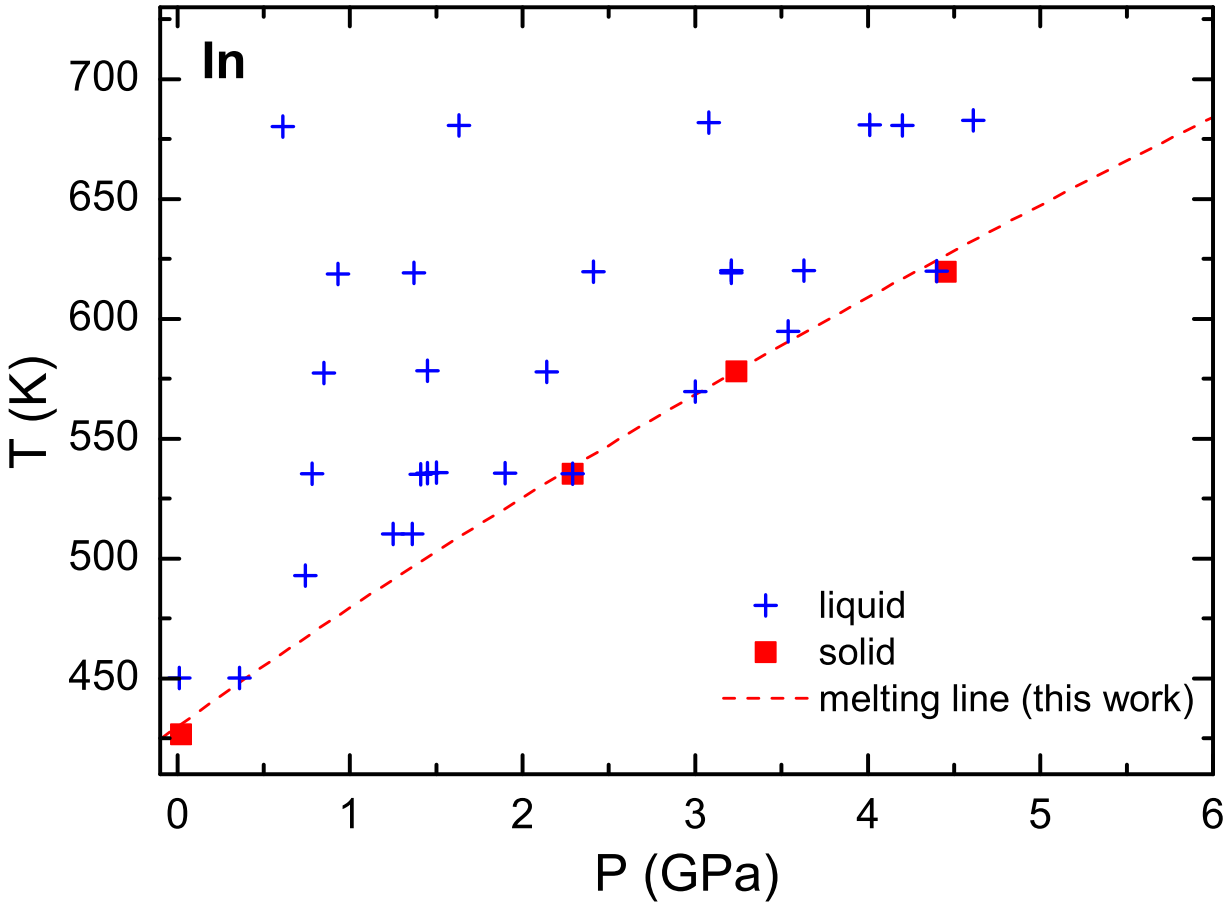

Supplementary Figure S2. $p-T$ location of the sound velocity measurements determined by phonon imaging in the liquid state (blue crosses) and in the solid state (red filled squares).

TABLE I. Raw data collected by the phonon imaging method in liquid state, from fit of $R(t)$ (depending on the run, some values, written in bold, have been fixed). Pressure p is determined by the SmSTB optical sensor and temperature T by a thermocouple glued in contact with one of the diamonds of the DAC ; m is an integer which accounts of the number of shots between generation and detection, v is adiabatic sound velocity, t_0 is the emergence time of the wave, e_0 is the sample thickness, and z_R is the acoustic Rayleigh length. Note that serie 1 was performed with $\lambda_0 = 950$ nm and serie 2 with $\lambda_0 = 800$ nm.

serie	run no	p (GPa)	T (K)	m	v (m/s)	t_0 (ns)	e_0 (μm)	z_R (μm)
1	1	0	296.05	*solid*				
1	2	0	580.65	**2**	2270	5.760	69.3	**16.2**
1	3	0	535.65	**2**	2268	5.338	68.3	**16.2**
1	4	0	495.65	**2**	2267	4.983	67.4	**16.2**
1	5	0.13	452.45	**2**	2283	4.710	67.3	**16.2**
1	6	0.13	426.75	*solid*				
2	1	0.36	450.15	**1**	2321	2.711	34.7	20.0
2	2	0.74	492.85	**1**	2376	2.643	35.4	16.4
2	3	0.74	492.85	**1**	2347	**2.670**	35.0	22.2
2	4	0.78	535.45	**1**	2356	**2.747**	35.4	21.0
2	5	0.85	577.35	**1**	2374	**2.750**	35.6	16.8
2	6	0.93	618.65	**1**	2356	**2.815**	35.5	19.0
2	7	1.37	619.15	**1**	2432	2.257	35.3	16.4
2	8	1.41	535.05	**1**	2453	**2.050**	35.1	21.9
2	9	1.45	535.55	**1**	2427	**2.050**	34.7	21.5
2	10	1.90	535.65	**1**	2524	**1.580**	34.9	17.2
2	11	2.14	577.85	**1**	2526	1.497	34.7	19.0
2	12	2.41	619.55	**1**	2555	1.376	34.8	15.0
2	13	3.21	619.25	**1**	2618	**0.884**	34.4	18.9
2	14	3.21	620.05	**1**	2641	0.836	34.6	18.0
2	15	3.24	578.15	*solid*				
2	16	3.54	594.85	**1**	2685	**0.500**	34.3	16.9
2	17	4.40	619.95	**1**	2748	0.133	34.0	16.4
2	18	4.45	619.55	*solid*				
2	19	3.63	620.05	**1**	2685	**0.533**	34.3	19.0
2	20	3.00	569.55	**1**	2643	0.609	34.0	16.0
2	21	2.29	535.45	*solid*				
2	22	1.50	535.95	**1**	2472	1.513	34.0	18.7
2	23	1.45	578.25	**1**	2435	1.573	33.7	15.1
2	24	1.36	510.35	**1**	2433	1.523	33.5	17.9
2	25	1.25	510.15	**1**	2415	**1.320**	32.8	20.0
2	26	0.01	450.15	**1**	2271	2.511	33.5	19.0
2	27	4.61	682.75	**0**	2735	**10.350**	27.5	14.7
2	28	3.08	681.85	**0**	2541	10.562	26.1	15.0
2	29	1.63	680.65	**0**	2437	**11.170**	26.5	15.0
2	30	0.61	680.25	**0**	2328	11.737	26.6	14.1
2	31	4.20	680.75	**0**	2685	**9.600**	25.0	14.9
2	32	4.01	680.95	**0**	2651	**9.720**	25.0	14.9

B. Sound velocity in liquid In - review as a function of T

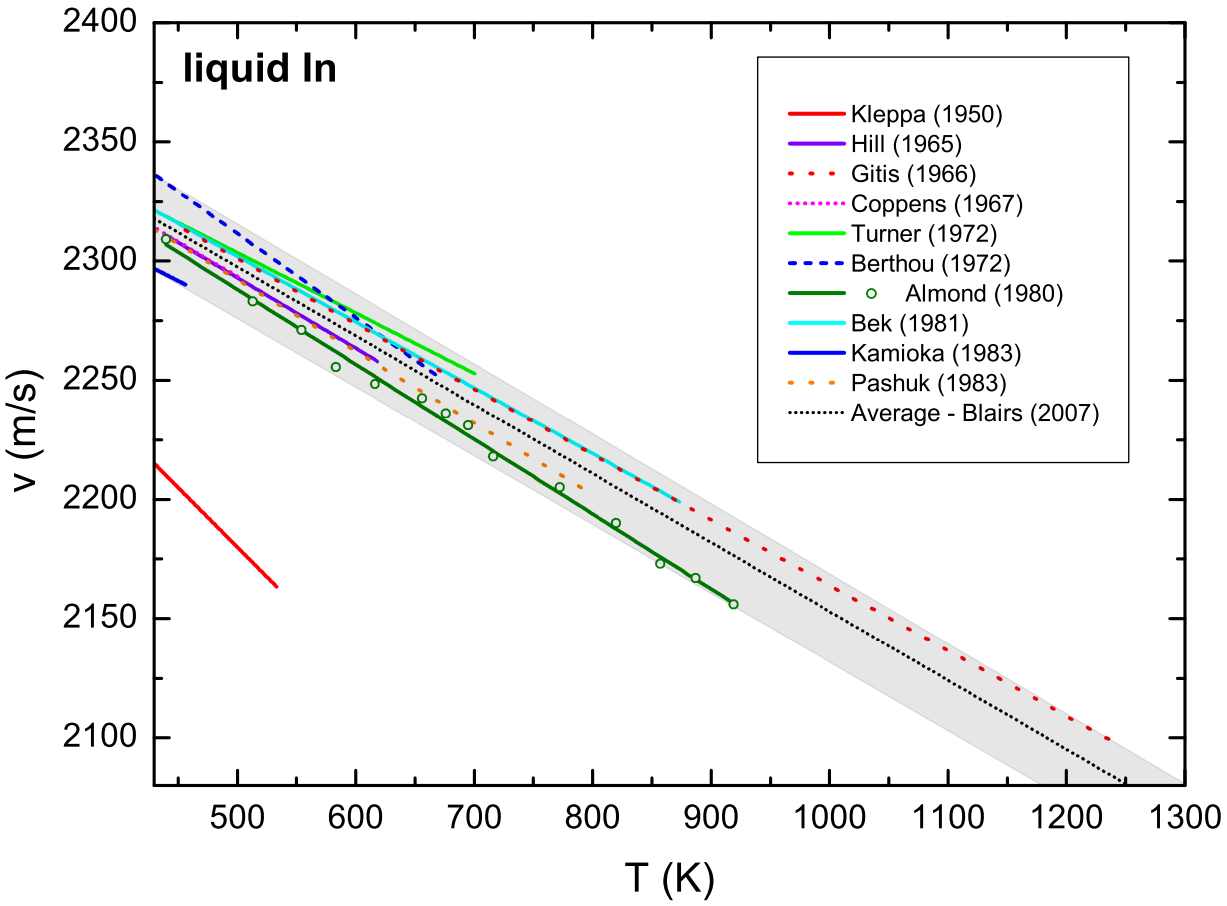

Supplementary Figure S3. Sound velocity in liquid In at ambient pressure and as a function of temperature, from melting temperature up to 1300 K. The selected references are from the review paper of Blairs [9], as well as the average trend described as $v(T) = 2442 - 0.289T$, where T is in K and v is in m/s. The grey area represents the dispersion of the literature data (Kleppa [31], Hill [26, 27], Gitis [22], Coppens [14], Turner [44], Berthou [8], Almond [2], Bek [7], Kamioka [30] and Pashuk [35]). *Note*: in the Table 24 of Blairs [9] the value "2448" (associated to Ref. [27] on first line) should be replaced by "2441".

C. Thermodynamic relations used to deduce EOS for liquid In

The adiabatic bulk modulus B_S is derived from $B_S = \rho v^2$ and from Blairs [9] the adiabatic sound velocity in m/s at ambient pressure is expressed versus temperature in K as

$$v(T) = 2442 - 0.298T. \tag{7}$$

According to Assael [4] the density in kg/m^3 obeys

$$\rho(T) = 7349.468 - 0.762T. \tag{8}$$

From the classical relation between isothermal and adiabatic stiffness [34]

$$s^T_{ijkl} = s^S_{ijkl} + T\alpha_{ij}\alpha_{kl}/\rho C_p \tag{9}$$

where $C_p(T)$ is the isobaric specific heat in J/mol/K, we obtain the expression between the isothermal and adiabatic bulk modulus

$$\frac{B_S}{B_T} = 1 + B_S\frac{T\alpha^2}{\rho C_p} = 1 + \frac{T\alpha^2 v^2}{C_p} = \gamma = 1 + \gamma_G\alpha T, \tag{10}$$

where γ is the heat capacity ratio and $\gamma_G = \alpha v^2/C_p$ the Grüneisen parameter.

Numerical values for B_S are then extracted from the $C_p(T)$ publication of Chapman [11] and modelled as in Ref.[5] in a polynomial form

$$C_p(T) = 32.513 - 1.033\ 10^{-2}T + 9.8459\ 10^{-6}T^2 - 33.463\ 10^{-10}T^3, \tag{11}$$

The thermal expansion

$$\alpha(T) = -\frac{1}{\rho}\left(\frac{\partial\rho}{\partial T}\right)_p$$

required in Eq. 10 and its first derivative, used for the following B'_T calculations, are obtained from Eq. 8

$$\alpha(T) = \frac{0.762}{7349.468 - 0.762T} \quad \text{and} \quad \left(\frac{\partial\alpha}{\partial T}\right)_p = \left(\frac{0.762}{7349.468 - 0.762T}\right)^2. \tag{12}$$

To fully determine the EOS, the two derivatives of the bulk modulus versus pressure

$$\left(\frac{\partial B_T}{\partial p}\right)_T = 1 + \frac{2B_T}{v}\left(\frac{\partial v}{\partial p}\right)_T - \frac{B_T}{\gamma}\left(\frac{\partial\gamma}{\partial p}\right)_T, \tag{13}$$

and temperature

$$\left(\frac{\partial B_T}{\partial T}\right)_p = -\alpha B_T + \frac{2B_T}{v}\left(\frac{\partial v}{\partial T}\right)_p - \frac{B_T}{\gamma}\left(\frac{\partial\gamma}{\partial T}\right)_p, \tag{14}$$

are required and then the following set of equations is needed [41, 45]:

$$\left(\frac{\partial\gamma}{\partial p}\right)_T = (\gamma - 1)\left[\frac{2}{\alpha}\left(\frac{\partial\alpha}{\partial p}\right)_T + \frac{2}{v}\left(\frac{\partial v}{\partial p}\right)_T - \frac{1}{C_p}\left(\frac{\partial C_p}{\partial p}\right)_T\right]. \tag{15}$$

$$\left(\frac{\partial\gamma}{\partial T}\right)_p = (\gamma - 1)\left[\frac{1}{T} + \frac{2}{v}\left(\frac{\partial v}{\partial p}\right)_T + \frac{2}{\alpha}\left(\frac{\partial\alpha}{\partial T}\right)_p - \frac{1}{C_p}\left(\frac{\partial C_p}{\partial T}\right)_p\right], \tag{16}$$

$$\left(\frac{\partial C_p}{\partial p}\right)_T = -\frac{T}{\rho}\left[\left(\frac{\partial\alpha}{\partial T}\right)_p + \alpha^2\right], \tag{17}$$

$$\left(\frac{\partial\alpha}{\partial p}\right)_T = \frac{1}{B_T^2}\left(\frac{\partial B_T}{\partial T}\right)_p, \tag{18}$$

Finally the Anderson–Grüneisen parameter involved in the thermal expansion modeling is derived as

$$\delta_T = -\frac{1}{\alpha B_T}\left(\frac{\partial B_T}{\partial T}\right)_p. \tag{19}$$

D. Comparison of the equations of state at ambient pressure

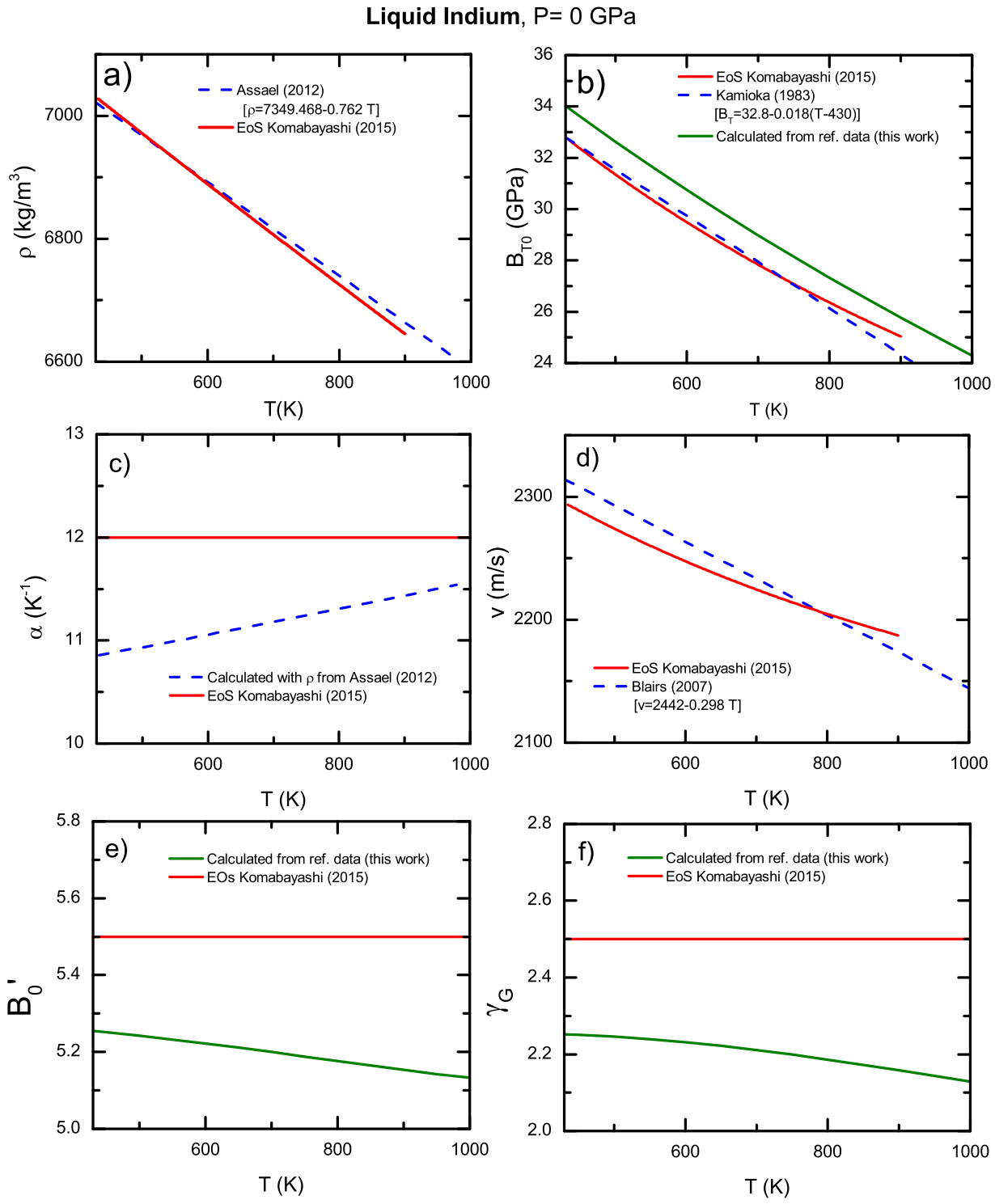

Supplementary Figure S4. Comparison between the thermodynamic data obtained by the EOS of Komabayashi [32] (red lines), the data from Assael [4], Blairs [9] and Kamioka [30] (blue dashed lines) and the data calculated from exact thermodynamical relations (green lines, see part II C). ρ is the density, B_{T0} the isothermal bulk modulus, α the thermal expansion, v the adiabatic sound velocity, B_0' the pressure derivative of the isothermal bulk modulus and γ_G is the Grüneisen parameter.

III. DETERMINATION OF THE MELTING CURVE

A. Additional figures

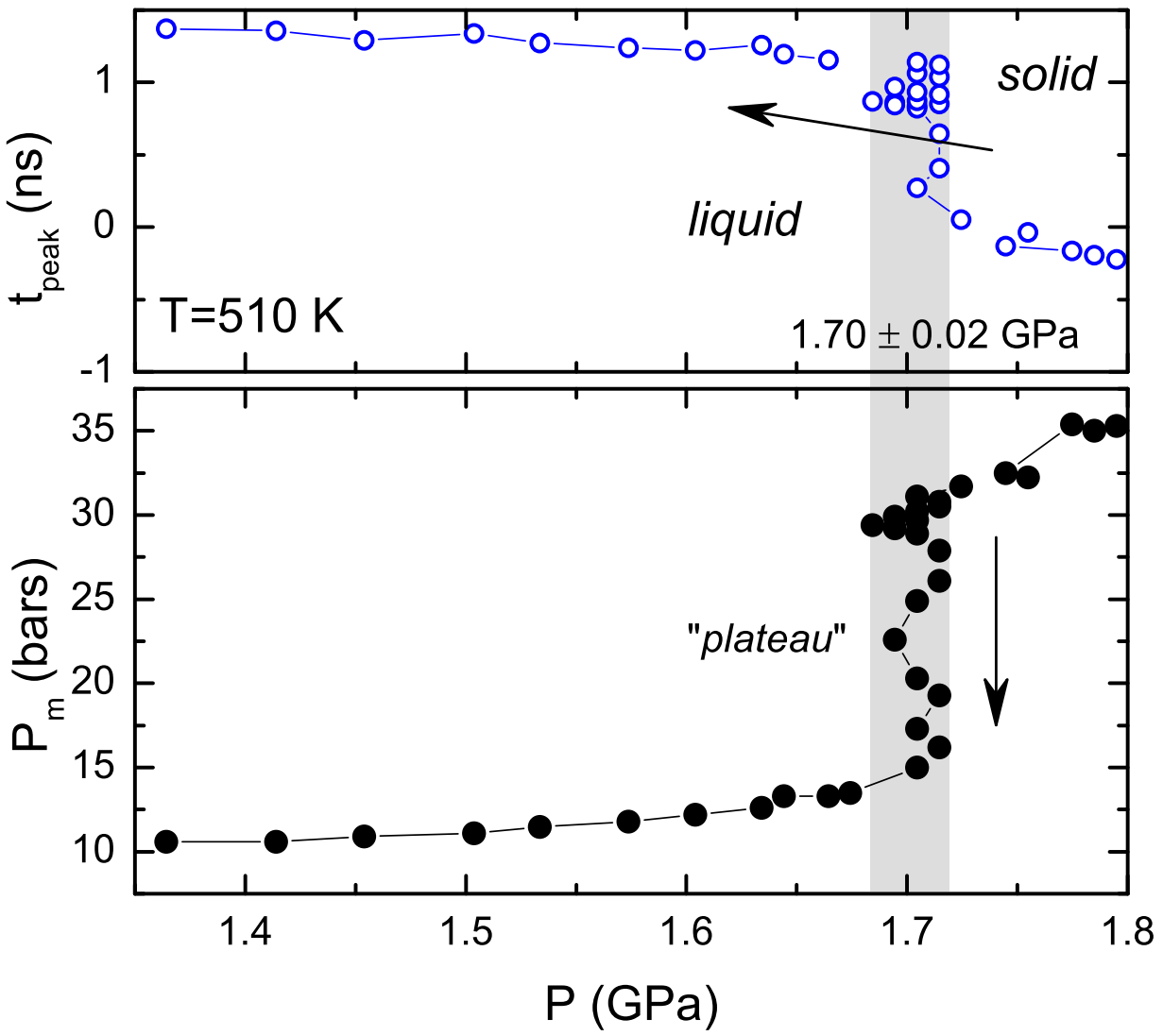

Supplementary Figure S5. Example of the "plateau" observed in the pressure membrane of the DAC as a function of the sample's pressure observed at the solid-liquid phase transition. This "plateau" is always observed at the phase transition, although with a variable extension.

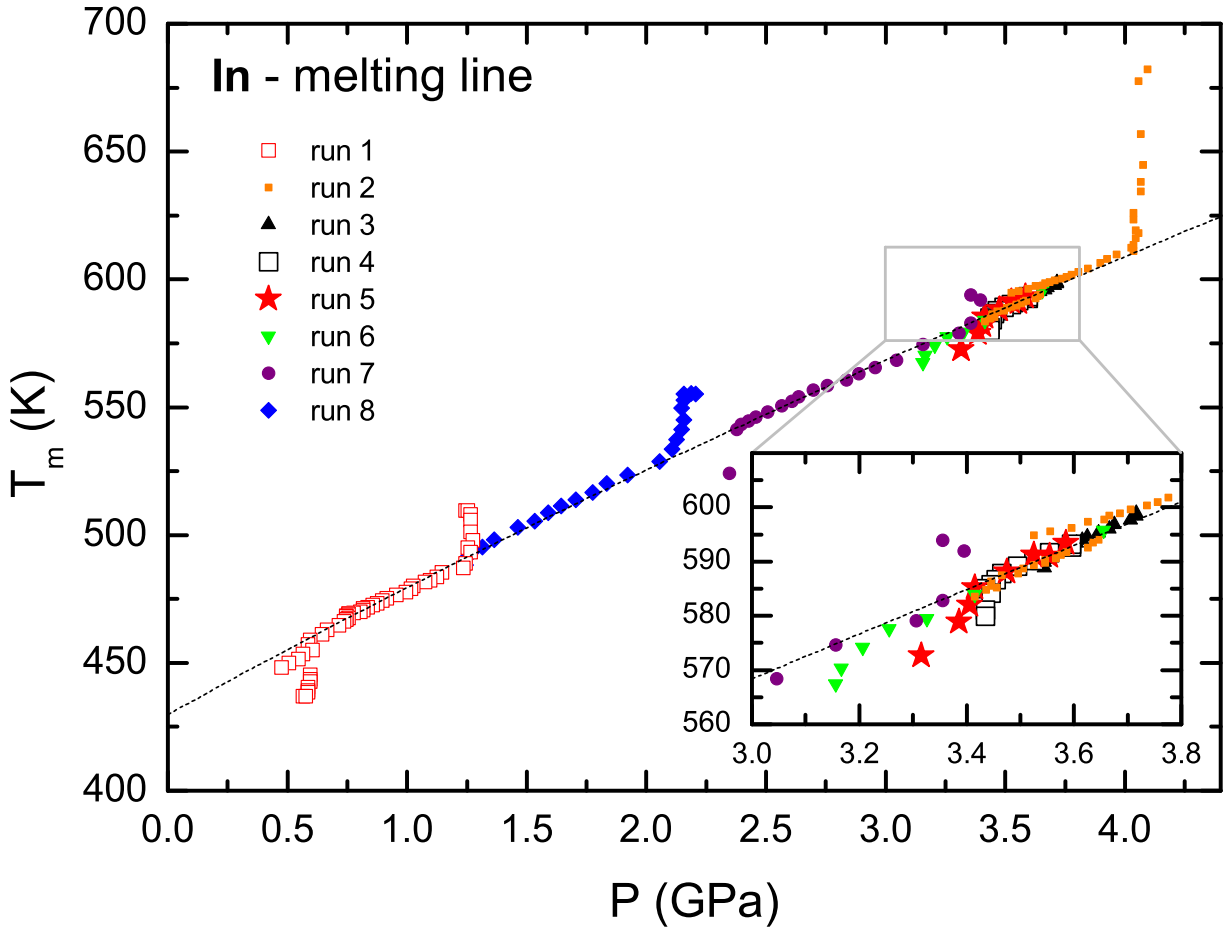

Supplementary Figure S6. Ensemble of the experimental runs performed to determine the melting curve in indium based on the liquid-solid equilibrium, with a zoom (inset) in the $p-T$ range where several data superimpose.

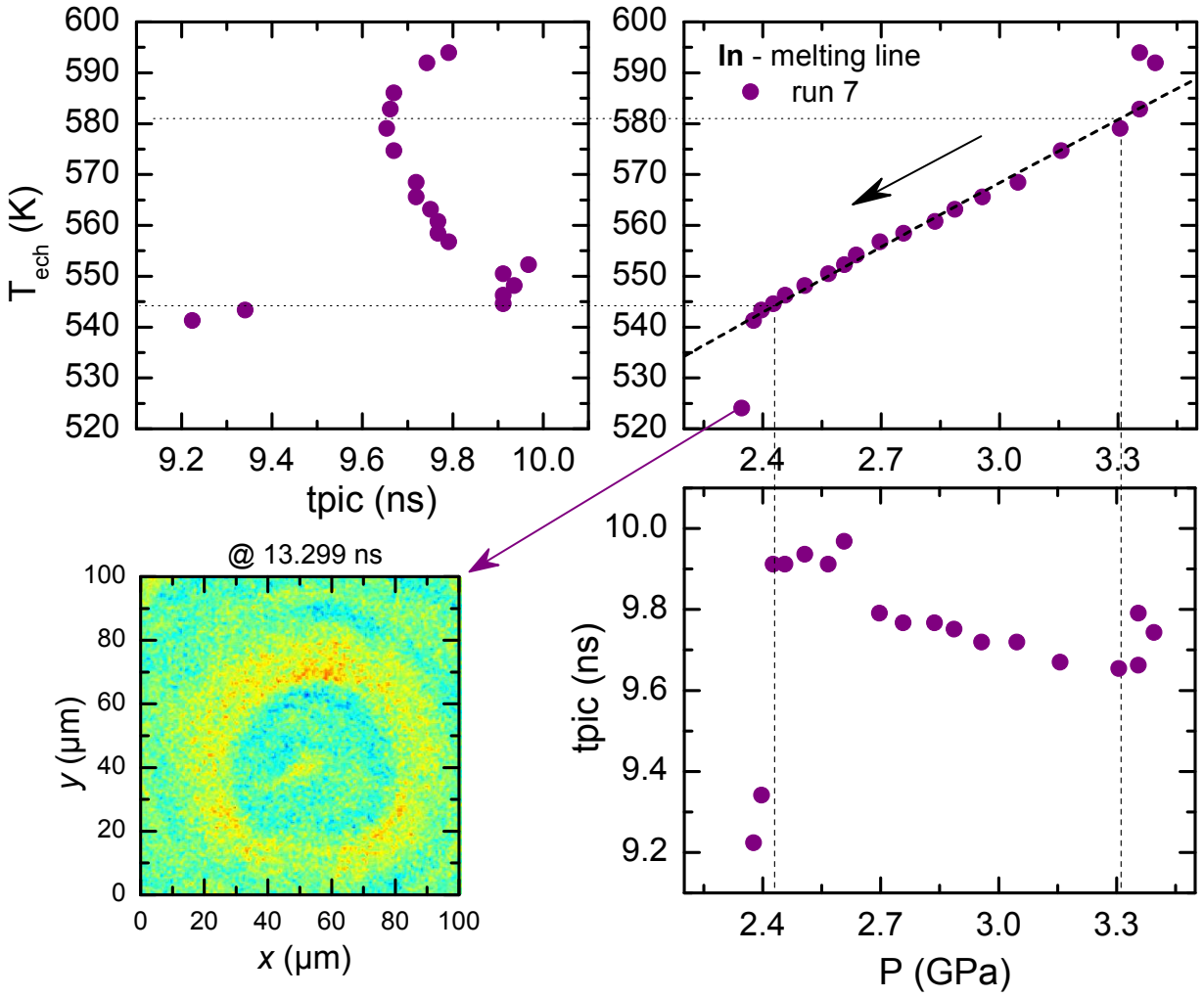

Supplementary Figure S7. $p-T$ data obtained in run 7 (upper right) compared to the melting curve determined by a Simon-Glatzel (dashed black line). The transition from liquid to solid at 544.4 K and 2.43 GPa is associated with a shift of the echo peak (upper left vs. T and bottom right vs. P). At the end of the run, the solid phase is confirmed by a non-circular pattern observed at the surface for a delay time of 13.299 ns (colored picture at the bottom left, the color scale goes from low values in blue to high values of the signal in red).

B. Slope of the melting curve from the Clausius-Clapeyron relation

This section presents the details of the calculation of κ_{ref}, the slope of the melting curve at ambient pressure from the Clausius-Clapeyron relation [37], where

$$\kappa_{ref} = \left(\frac{dT_M}{dp}\right)_{p=0} = \frac{T_M^0(V_{m,liq} - V_{m,sol})}{\Delta H_{m,M}}. \tag{20}$$

The terms appearing in this Equation are defined below.

1. *Physical and thermodynamical data*

The melting temperature at ambient pressure is [1, 38]

$$T_M^0 = 429.748500(341)\ K. \tag{21}$$

The molar mass of indium is $M = 114.818$ g/mol [13]. Measurement of Archer *et al* [3] are considered the most accurate and are the most used value among the documented standards [1] for the the molar enthalpy of fusion (or melting) $\Delta H_{m,M}$. This value, with an uncertainty at 2σ, is $\Delta H_{m,M} = 28.6624(76)$ J/g *i. e.*

$$\Delta H_m = 3290.96(44)\ J/mol \tag{22}$$

with an uncertainty this time at 1σ.

2. Liquid state

The density in liquid indium at ambient pressure as a function of temperature is carefully reviewed by Assael [4], and it is described by the equation

$$\rho_{liq}(T) = 7022 - 0.762\,(T - 429.748)$$

with an uncertainty of 0.5% at the 95% confidence level (2 σ) and T in K, ρ in kg/m^3. With a 1 σ uncertaincy, we get

$$\rho_{liq}(T_M^0) = 7022(18)\ kg/m^3 \ \ i.e.\ \ V_{m,liq} = \frac{M}{\rho_{liq}} = 16.35\ 10^{-6}\ m^3/mol$$

and

$$\delta V_{m,liq} = V_{m,liq}\frac{\delta\rho_{liq}}{\rho_{liq}} = 40.88\ 10^{-9}\ m^3/mol.$$

3. Solid state

To determine the density at T_M^0 in the solid In at ambient pressure as a function of temperature, a linear fit $\rho_{sol}(T) = aT + b$ is performed to the literature data obtained in the solid phase (see Fig. S8), yielding to b = 7308.9(39) kg/m^3 and a = -0.69(4) kg/m^3/C.

The density at T_M^0 is then

$$\rho_{sol}(T_M^0) = aT_M^0 + b = 7201\ kg/m^3,$$

with the uncertainty

$$\delta\rho_{sol}(T_M^0) = \sqrt{\left(T_M^0\delta a\right)^2 + \left(a\delta T_M^0\right)^2 + \delta b^2} = 7\ kg/m^3,$$

and finally

$$V_{m,sol} = \frac{M}{\rho_{sol}} = 15.94\ 10^{-6}\ m^3/mol,$$

$$\delta V_{m,sol} = V_{m,sol}\frac{\delta\rho_{sol}}{\rho_{sol}} = 16.20\ 10^{-9}\ m^3/mol.$$

4. Difference of the molar volumes

The difference of the molar volumes between the solid and the liquid at the melting temperature T_M^0 is $\Delta V_m = V_{m,liq} - V_{m,sol}$ with uncertainties estimated from error propagation $\delta\Delta V_m = \sqrt{\left(\delta V_{m,liq}\right)^2 + \left(\delta V_{m,sol}\right)^2}$, so that

$$\Delta V_m = 406(36)\ 10^{-9}\ m^3/mol.$$

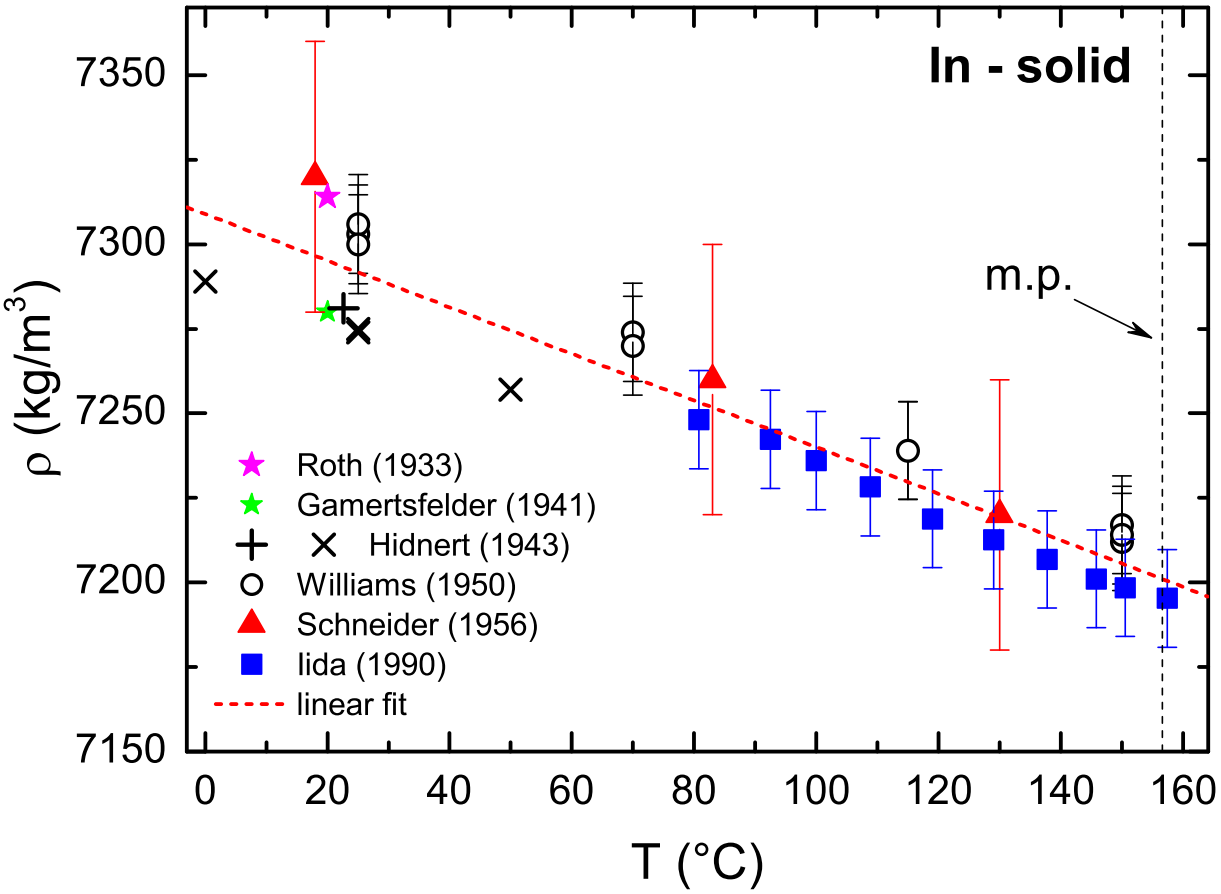

Supplementary Figure S8. Solid indium density at ambient pressure versus temperature. Data are from Roth [39], Gamertsfelder [20], Hidnert & Blair [25] obtained from a 250-mm rod sample of cast In (black plus) and from a 200-mm rod (black crosses), Williams [46], Schneider [40] and Iida [29]. The red dashed line is a instrumental weighted linear regression through the experimental points. The density of the solid phase at room temperature (20 C or 293.15 K) is 7295(4) kg/m^3.

5. The Clausius-Clapeyron relation at ambient pressure

Finally κ_{ref} is obtained as

$$\kappa_{ref} = \frac{T_M^0 \Delta V_m}{\Delta H_{m,M}} = 53.1 \ K/GPa.$$

with a relative uncertainty $\delta\kappa_{ref}$ given by

$$\frac{\delta\kappa_{ref}}{\kappa_{ref}} = \sqrt{\left(\frac{\delta T_M^0}{T_M^0}\right)^2 + \left(\frac{\delta \Delta H_{m,M}}{\Delta H_{m,M}}\right)^2 + \left(\frac{\delta \Delta V_m}{\Delta V_m}\right)^2} = 9.0\%$$

The principal contribution to this uncertainty comes from the $\delta\Delta V_m/\Delta V_m$ term, which represents the small difference in density between solid and liquid phases at melting with respect to the uncertainty of the density measurements.

To conclude, the resulting value is

$$\kappa_{ref} = 53.1(48) \ K/GPa.$$

The comparison of this result to the value provided by Höhne *et al* [28], κ = 50.7(30) K/GPa, shows a good agreement within the mutual uncertainties. In addition, as a byproduct of this study, the density of solid In at ambient temperature (298.15 K) is revised to

$$\rho(298.15 \ K) = 7292(4) \ kg/m^3$$

.

C. Correction of the melting curve from Dudley *et al*

The original calibration curve used by Dudley [19] is shown in Fig. S9 below. They used a pressure value of 24.8 katm for the solid-solid phase transition Bi I-II at ambient temperature, and 77.4 katm for Ba I-II, from the work of Bridgman [10]. Their calibration curve is linear $p(\text{katm}) = a\, p(\text{psi})$, with $a = 12.89(9)\ 10^{-3}$ psi/katm.

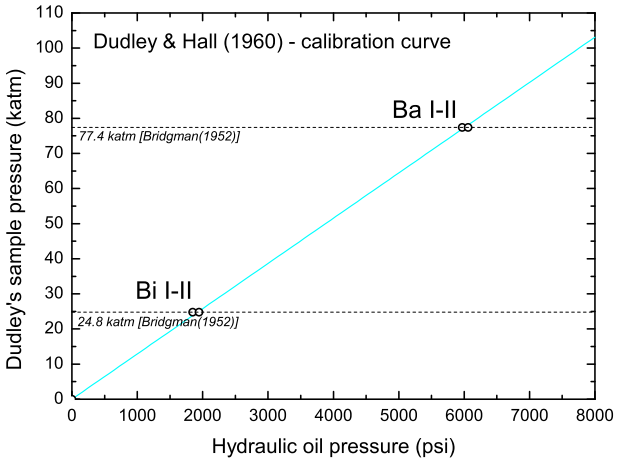

Supplementary Figure S9. Original calibration curve used in the work of Dudley & Hall [19].

However, this calibration curve has to be corrected as the pressure value of the Ba I-II transition given by Bridgman was discussed and revised in following studies. The seminal work of Haygarth *et al* [24] gives $p_{Ba\ I-II} = 5.50(5)$ GPa at 295.15 K. Decker made a careful review (see Table 7 in [17] and the associated discussion) including the data of Haygarth and some other works, and he gives $p_{Ba\ I-II} = 5.53(12)$ GPa at 298.15 K. Concerning the transition Bi I-II, Getting [21] gives a reference value of $p_{Bi\ I-II} = 2.520(5)$ GPa at 298.15 K.

The calibration curve between press load and sample pressure is in most cases nonlinear, as seen in Fig. 5 from Ref [23], or in Fig. 4 from ref [42] and the curve depends on the tetrahedron size (see Fig. 8 in ref.[6]).

Based on these features, we propose the following *ad hoc* non linear functional form

$$p\,(\text{GPa}) = (1.4 + 0.053\, p\ (\text{katm}))\left(1 - e^{-p\ (\text{katm})/10}\right), \tag{23}$$

which is shown in Fig. S10.

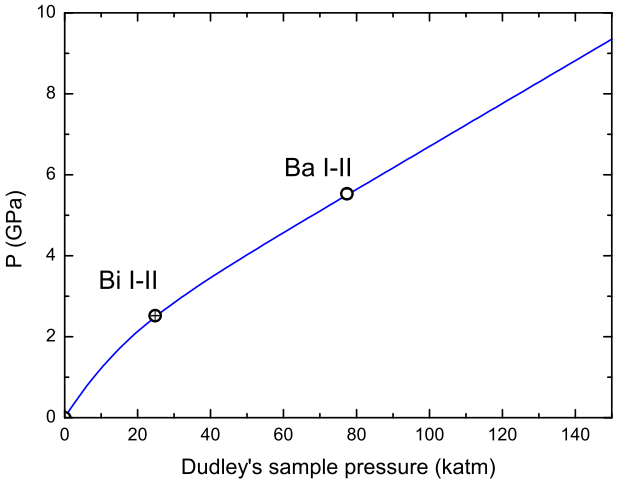

Supplementary Figure S10. Non-linear correction applied to the sample pressure of Dudley [19].

[1] Haruka Abe. National standard and new reference material for specific heat capacity measurements. *Analytical Sciences*, 37(1):201–210, 2021.

[2] DP Almond and S Blairs. Ultrasonic speed, compressibility, and structure factor of liquid cadmium and indium. *The Journal of Chemical Thermodynamics*, 12(12):1105–1114, 1980.

[3] Donald G Archer and Steffen Rudtsch. Enthalpy of fusion of indium: a certified reference material for differential scanning calorimetry. *Journal of Chemical & Engineering Data*, 48(5):1157–1163, 2003.

[4] Marc J Assael, Ivi J Armyra, Juergen Brillo, Sergei V Stankus, Jiangtao Wu, and William A Wakeham. Reference data for the density and viscosity of liquid cadmium, cobalt, gallium, indium, mercury, silicon, thallium, and zinc. *Journal of Physical and Chemical Reference Data*, 41(3):033101, 2012.

[5] Simon Ayrinhac. Heat capacity ratio in liquids at high pressure. *Journal of Applied Physics*, 129(18):185903, 2021.

[6] MD Banus and Susan D Nye. Efficiency in a tetrahedral-anvil press as related to anvil and pyrophyllite size. *Review of Scientific Instruments*, 35(10):1319–1323, 1964.

[7] R Bek, E Nold, and S Steeb. Röntgen-Beugungs-untersuchungen an Bi-In-Schmelzen (in german) : X-Ray diffraction experiments with Bi-In-melts. *Zeitschrift für Naturforschung A*, 36(2):150–153, 1981.

[8] P-E Berthou and R Tougas. The compressibilities of liquid Sn-Tl, In-Bi, Sn-In, Bi-Sb, and Bi-Cd-Tl alloys. *Metallurgical and Materials Transactions B*, 3(1):51–54, 1972.

[9] S Blairs. Review of data for velocity of sound in pure liquid metals and metalloids. *International materials reviews*, 52(6):321–344, 2007.

[10] P. W. Bridgman. The resistance of 72 elements, alloys and compounds to 100000 Kg/cm^2. *Proceedings of the American Academy of Arts and Sciences*, 81:167, March 1952.

[11] Thomas W Chapman. The heat capacity of liquid metals. *Materials Science and Engineering*, 1(1):65–69, 1966.

[12] JC Chervin, B Canny, and M Mancinelli. Ruby-spheres as pressure gauge for optically transparent high pressure cells. *International Journal of High Pressure Research*, 21(6):305–314, 2001.

[13] Tyler B. Coplen, Norman E. Holden, Tiping Ding, Harro A.J. Meijer, Jochen Vogl, and Xiangkun Zhu. The table of standard atomic weights—an exercise in consensus. *Rapid Communications in Mass Spectrometry*, n/a(n/a):e8864.

[14] Alan B. Coppens, Robert T. Beyer, and Joseph Ballou. Parameter of nonlinearity in fluids III. Values of sound velocity in liquid metals. *The Journal of the Acoustical Society of America*, 41(6):1443–1448, 1967.

[15] F Datchi, A Dewaele, P Loubeyre, R Letoullec, Y Le Godec, and B Canny. Optical pressure sensors for high-pressure–high-temperature studies in a diamond anvil cell. *High Pressure Research*, 27(4):447–463, 2007.

[16] F. Datchi, R. Le Toullec, and P. Loubeyre. Improved calibration of the SrB_4O_7:Sm^{2+} optical pressure gauge: Advantages at very high pressures and high temperatures. *Journal of Applied Physics*, 81(8):3333–3339, 1997.

[17] Daniel Lorenzo Decker, WA Bassett, L Merrill, HT Hall, and JD Barnett. High-pressure calibration: A critical review. *Journal of Physical and Chemical Reference Data*, 1(3):773–836, 1972.

[18] Peter I Dorogokupets and Artem R Oganov. Ruby, metals, and mgo as alternative pressure scales: A semiempirical description of shock-wave, ultrasonic, x-ray, and thermochemical data at high temperatures and pressures. *Physical Review B*, 75(2):024115, 2007.

[19] J Duane Dudley and H Tracy Hall. Experimental fusion curves of indium and tin to 105000 atmospheres. *Physical Review*, 118(5):1211, 1960.

[20] Carl Gamertsfelder. Atomic distributions in liquid elements. *The Journal of Chemical Physics*, 9(6):450–457, 1941.

[21] IC Getting. New determination of the bismuth i-ii equilibrium pressure: A proposed modification to the practical pressure scale. *Metrologia*, 35(2):119, 1998.

[22] MB Gitis and IG Mikhailov. Correlation of the velocity of sound and electrical conductivity in liquid metals. *Sov. Phys. Acoust*, 12:14–17, 1966.

[23] H Tracy Hall and Leo Merrill. Some high pressure studies on ytterbium. *Inorganic Chemistry*, 2(3):618–624, 1963.

[24] JC Haygarth, IC Getting, and GC Kennedy. Determination of the pressure of the barium i-ii transition with single-stage piston-cylinder apparatus. *Journal of Applied Physics*, 38(12):4557–4564, 1967.

[25] Peter Hidnert and Mary Grace Blair. Thermal expansivity and density of indium. *Journal of Research of the National Bureau of Standards*, 30:427, 1943.

[26] J. E. Hill and A. L. Ruoff. Velocity of sound measurements in liquid metals. *Review of Scientific Instruments*, 36(10):1465–1472, 1965.

[27] J.E. Hill and A.L. Ruoff. Temperature dependence of the velocity of sound in some liquid metals and eutectic alloys. *The Journal of Chemical Physics*, 43(6):2150–2151, 1965.

[28] GWH Höhne, W Dollhopf, K Blankenhorn, and PU Mayr. On the pressure dependence of the heat of fusion and melting temperature of indium. *Thermochimica acta*, 273:17–24, 1996.

[29] Takamichi Iida, Yoshifumi Kita, Yukio Kikuya, Tadashi Kirihara, and Zen-ichiro Morita. Densities of Ga-In and In-Sn alloys in the solid and liquid states. *Journal of non-crystalline solids*, 117:567–570, 1990.

[30] Hiroaki Kamioka. Change of ultrasonic wave velocity in indium near the melting point. *Journal of the Physical Society of Japan*, 52(8):2784–2789, 1983.

[31] OJ Kleppa. Ultrasonic velocities of sound in some metallic liquids. adiabatic and isothermal compressibilities of liquid metals at their melting points. *The Journal of Chemical Physics*, 18:1331, 1950.

[32] Tetsuya Komabayashi, Jinya Kato, Kei Hirose, Satoshi Tsutsui, Saori Imada, Yoichi Nakajima, and Alfred QR Baron.

Temperature dependence of the velocity-density relation for liquid metals under high pressure: Implications for the Earth's outer core. *American Mineralogist*, 100(11-12):2602–2609, 2015.

[33] DE McCumber and MD Sturge. Linewidth and temperature shift of the r lines in ruby. *Journal of Applied Physics*, 34(6):1682–1684, 1963.

[34] HJ McSkimin, P Andreatch Jr, and RNL Thurston. Elastic moduli of quartz versus hydrostatic pressure at 25 and- 195.8 c. *Journal of Applied Physics*, 36(5):1624–1632, 1965.

[35] EG Pashuk and BP Pashaev. Temperature dependence of superround velocity and related volumetric dependence of the young modulus of some metals. *Teplofizika Vysokikh Temperatur*, 21(3):479–483, 1983.

[36] Ge J Piermarini, S Block, JD Barnett, and RA Forman. Calibration of the pressure dependence of the r 1 ruby fluorescence line to 195 kbar. *Journal of Applied Physics*, 46(6):2774–2780, 1975.

[37] Jean-Paul Poirier. *Introduction to the Physics of the Earth's Interior*. Cambridge University Press, 2000.

[38] H Preston-Thomas. The international temperature scale of 1990 (ITS-90). *metrologia*, 27(1):3–10, 1990.

[39] WA Roth, Ingrid Meyer, and Hans Zeumer. Atom-, schmelz-und umwandlungswärmen von gallium, indium und thallium. *Zeitschrift für anorganische und allgemeine Chemie*, 214(3):309–320, 1933.

[40] A Schneider and G Heymer. Die temperaturabhängigkeit der molvolumina der phasen natl und licd. *Zeitschrift für anorganische und allgemeine Chemie*, 286(3-4):118–135, 1956.

[41] George H. Shaw and D. A. Caldwell. Device for measuring sound speeds in reactive liquids at high pressure and temperature. *Review of Scientific Instruments*, 56(7):1402–1408, 1985.

[42] Mitsuhiko Shimada. The effect of repeated loading on the generated pressure in a girdle high pressure apparatus. *Contributions of the Geophysical Institute, Kyoto University*, 14:49–57, 1974.

[43] K Syassen. Ruby under pressure. *High Pressure Research*, 28(2):75–126, 2008.

[44] Robert Turner, ED Crozier, and JF Cochran. A new technique for measuring the velocity of sound in liquid metals. *Canadian Journal of Physics*, 50(22):2735–2740, 1972.

[45] Emmerich Wilhelm. What you always wanted to know about heat capacities, but were afraid to ask. *Journal of Solution Chemistry*, 39(12):1777–1818, 2010.

[46] DD Williams and RR Miller. Densities of liquid and solid indium. *Journal of the American Chemical Society*, 72(8):3821–3821, 1950.